Seipin localizes at endoplasmic-reticulum-mitochondria contact sites to control mitochondrial calcium import and metabolism in adipocytes

Yoann Combot, Veijo T. Salo, Gilliane Chadeuf, Maarit Hölttä, Katharina Ven, Ilari Pulli, Simon Ducheix, Claire Pecqueur, Ophélie Renoult, Behnam Lak, et al.

Cell Reports

Article

Seipin localizes at endoplasmic-reticulum-mitochondria contact sites to control mitochondrial calcium import and metabolism in adipocytes

Graphical abstract

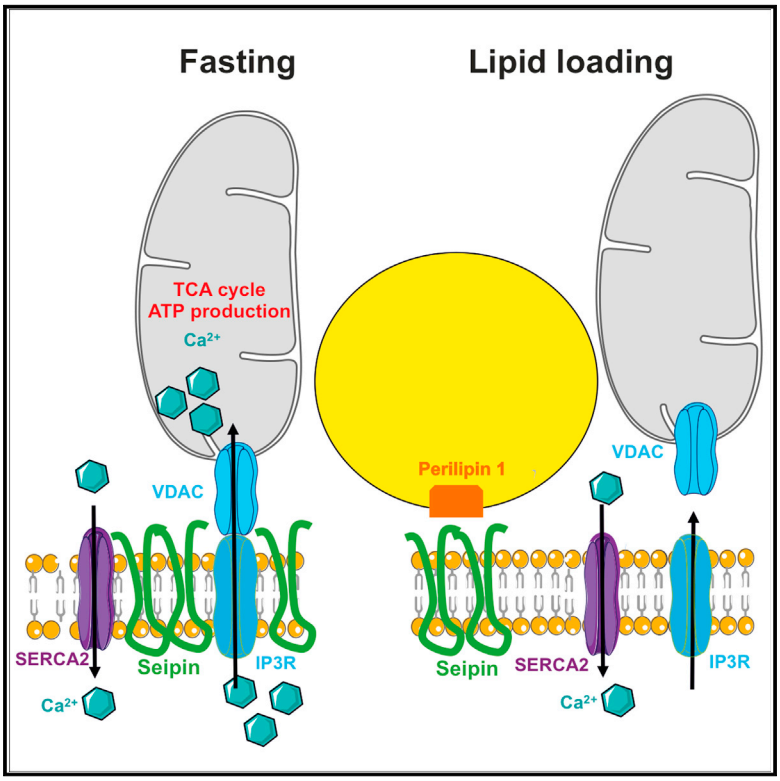

Highlights

- Seipin is enriched at ER-MAMs
- Seipin interacts with MAM calcium regulators in a nutritionally regulated manner
- Adipocyte seipin deficiency impairs mitochondrial calcium import and ATP production
- Inducible seipin removal from adipose tissue leads to rapid mitochondrial dysfunction

Authors

Yoann Combot, Veijo T. Salo, Gilliane Chadeuf, ..., Abdelhalim Larhlimi, Elina Ikonen, Xavier Prieur

Correspondence

elina.ikonen@helsinki.fi (E.I.), xavier.prieur@univ-nantes.fr (X.P.)

In brief

Combot et al. demonstrate that seipin is enriched at ER-mitochondria contact sites and that seipin deficiency leads to defective mitochondrial calcium import accompanied by a reduction in ATP production. In mice, inducible seipin deletion from adipocytes leads to early mitochondrial dysfunction, which probably contributes to the pathogenesis of seipin-related lipodystrophy.

Combot et al., 2022, Cell Reports *38*, 110213
January 11, 2022
https://doi.org/10.1016/j.celrep.2021.110213

CellPress

Cell Reports

CellPress
OPEN ACCESS

Article

Seipin localizes at endoplasmic-reticulum-mitochondria contact sites to control mitochondrial calcium import and metabolism in adipocytes

Yoann Combot,[1,15] Veijo T. Salo,[2,3,15] Gilliane Chadeuf,[1] Maarit Hölttä,[2,3] Katharina Ven,[2,3] Ilari Pulli,[4] Simon Ducheix,[1] Claire Pecqueur,[5] Ophélie Renoult,[5] Behnam Lak,[6] Shiqian Li,[2,3] Leena Karhinen,[2,3] Ilya Belevich,[6] Cedric Le May,[1] Jennifer Rieusset,[7] Soazig Le Lay,[1,8] Mikael Croyal,[1,9,10] Karim Si Tayeb,[1] Helena Vihinen,[6] Eija Jokitalo,[6] Kid Törnquist,[3,4] Corinne Vigouroux,[11,12] Bertrand Cariou,[13] Jocelyne Magré,[1] Abdelhalim Larhlimi,[14] Elina Ikonen,[2,16,*] and Xavier Prieur[1,16,17,*]

[1]Université de Nantes, CNRS, INSERM, l'institut du thorax, 44000 Nantes, France
[2]Department of Anatomy and Stem Cells and Metabolism Research Program, Faculty of Medicine, University of Helsinki, Helsinki, Finland
[3]Minerva Foundation Institute for Medical Research, Helsinki, Finland
[4]Faculty of Science and Engineering, Cell Biology, Åbo Akademi University, Turku, Finland
[5]Université de Nantes, CNRS, INSERM, CRCINA, 44000 Nantes, France
[6]Institute of Biotechnology, Helsinki Institute of Life Science, University of Helsinki, Helsinki, Finland
[7]Laboratoire de Recherche en Cardiovasculaire, Métabolisme, Diabétologie et Nutrition (CarMeN), INSERM U1060, INRA U1397, Institut National des Sciences Appliquées-Lyon, Université Claude Bernard Lyon1, Oullins, Lyon, France
[8]Univ Angers, SFR ICAT, 49000 Angers, France
[9]CRNH-Ouest Mass Spectrometry Core Facility, 44000 Nantes, France
[10]Université de Nantes, CHU Nantes, Inserm, CNRS, SFR Santé, Inserm UMS 016, CNRS UMS 3556, 44000 Nantes, France
[11]Sorbonne University, Inserm UMR_S938, Saint-Antoine Research Centre, Institute of Cardiometabolism and Nutrition, Paris, France
[12]Assistance Publique-Hôpitaux de Paris, Saint-Antoine University Hospital, National Reference Center for Rare Diseases of Insulin Secretion and Insulin Sensitivity (PRISIS), Department of Molecular Biology and Genetics and of Endocrinology, Diabetology and Reproductive Endocrinology, Paris, France
[13]Université de Nantes, CHU Nantes, CNRS, INSERM, l'institut du thorax, 44000 Nantes, France
[14]LS2N, UMR6004, CNRS, Université de Nantes, Nantes, France
[15]These authors contributed equally
[16]These authors contributed equally
[17]Lead contact
*Correspondence: elina.ikonen@helsinki.fi (E.I.), xavier.prieur@univ-nantes.fr (X.P.)
https://doi.org/10.1016/j.celrep.2021.110213

SUMMARY

Deficiency of the endoplasmic reticulum (ER) protein seipin results in generalized lipodystrophy by incompletely understood mechanisms. Here, we report mitochondrial abnormalities in seipin-deficient patient cells. A subset of seipin is enriched at ER-mitochondria contact sites (MAMs) in human and mouse cells and localizes in the vicinity of calcium regulators SERCA2, IP3R, and VDAC. Seipin association with MAM calcium regulators is stimulated by fasting-like stimuli, while seipin association with lipid droplets is promoted by lipid loading. Acute seipin removal does not alter ER calcium stores but leads to defective mitochondrial calcium import accompanied by a widespread reduction in Krebs cycle metabolites and ATP levels. In mice, inducible seipin deletion leads to mitochondrial dysfunctions preceding the development of metabolic complications. Together, these data suggest that seipin controls mitochondrial energy metabolism by regulating mitochondrial calcium influx at MAMs. In seipin-deficient adipose tissue, reduced ATP production compromises adipocyte properties, contributing to lipodystrophy pathogenesis.

INTRODUCTION

Seipin is an endoplasmic reticulum (ER) transmembrane protein highly expressed in the adipose tissue and in the brain (Payne et al., 2008). Biallelic null mutations in *BSCL2*, the seipin-encoding gene, are responsible for a rare and severe primary adipocyte dysfunction syndrome, Berardinelli-Seip congenital lipodystrophy (BSCL), characterized by a lack of adipose tissue and severe metabolic complications (i.e., insulin resistance, diabetes, hypertriglyceridemia, liver steatosis) (Magre et al., 2001). Seipin-deficient (SKO) mice are lipoatrophic and develop diabetes and liver steatosis (Chen et al., 2012; Cui et al., 2011; Prieur et al., 2013). In addition, SKO mice are intolerant to fasting, display metabolic inflexibility and impaired thermogenesis (Dollet et al., 2016), and develop diabetic cardiomyopathy (Joubert et al., 2017). Seipin deficiency in the developing adipocyte, using

adiponectin-Cre constructions (McIlroy et al., 2018) or AP2-Cre mice (Liu et al., 2014), leads to lipodystrophy. Finally, inducible seipin deficiency obtained through ERT2-Adipoq-CRE-dependent recombination leads to progressive white adipose tissue loss associated with increased basal adipocyte lipolysis (Zhou et al., 2015). Although these studies highlight a critical role of seipin in mature adipocytes, its function therein remains largely unknown.

Studies in yeast (Fei et al., 2008, 2011; Szymanski et al., 2007) and human lymphocytes (Boutet et al., 2009) have shown that seipin is crucial for normal lipid droplet (LD) morphology. Seipin is localized at ER-LD contact sites during LD biogenesis and is needed for the delivery of lipid and protein cargo to nascent LDs (Wang et al., 2016). Recently, we demonstrated that seipin interacts with triglycerides (TGs) and helps the flow of TG to the LD by maintaining functional ER-LD contacts and counteracting LD ripening (Prasanna et al., 2021; Salo et al., 2016, 2019). Consistently, seipin interacts with several ER enzymes involved in TG synthesis such as AGPAT2 (Talukder et al., 2015), lipin1 (Sim et al., 2012), and GPAT3 (Pagac et al., 2016), and co-operates with Pet10, the yeast ortholog of perilipin 1(Gao et al., 2017).

In addition to its role in LD homeostasis, *Drosophila* seipin has been shown to interact with the sarco/ER calcium ATPase pump 2 (SERCA2) and *dSeipin* mutant fat cells display decreased ER calcium levels (Bi et al., 2014). Further studies have shown that the fat bodies of *dSeipin* mutant flies also exhibit reduced mitochondrial calcium levels and respiratory ability (Ding et al., 2018). Whether seipin regulates ER or mitochondrial calcium metabolism and mitochondrial activity in other organisms is not known. Furthermore, how seipin regulates ER/mitochondrial calcium exchange and how its involvement in lipid and calcium handling may be reconciled, have not been explored.

Here, we investigated the role of seipin in controlling mitochondrial homeostasis starting from the observation that BSCL2 patients' cells display abnormal mitochondrial morphology and function. Using human epidermoid carcinoma A431 and murine pre-adipocyte 3T3-L1 cells, we determined the subcellular localization of seipin and its interaction partners in different nutritional states. This revealed that seipin is enriched at ER-mitochondria contact sites, together with calcium regulatory proteins. We also generated mice with an adipocyte-specific conditional deletion of seipin and found evidence for early and severe alterations of mitochondrial properties *in vivo*.

RESULTS

Abnormal mitochondrial morphology and reduced oxygen consumption in BSCL2 patients' cells

We have previously reported abnormal LDs in lymphoblastoid cells isolated from lipodystrophic BSCL2 patients (Boutet et al., 2009). When analyzing the lymphoblastoid cells using transmission electron microscopy (TEM), we noticed that mitochondrial morphology is also perturbed in three out of the four BSCL2 patient lymphoblasts studied, as demonstrated by dilated and disorganized cristae and matrix granules (Figures 1A–1C), which are signs of mitochondrial injury (Solenski et al., 2002). No systematic morphological defects in other organelles, such as the ER, Golgi, and endosomal structures, were observed in the BSCL2 patient lymphoblasts by TEM. The patient cells also displayed a lower oxygen consumption rate (OCR) compared with controls, indicating mitochondrial dysfunction (Figure 1D). Decreased OCR was also characteristic to seipin knockout A431 cells previously characterized by us (Salo et al., 2016), and this could be corrected by seipin re-expression (Figure 1E). These findings demonstrate, in two different human cell types, that seipin deficiency compromises mitochondrial function.

Seipin is associated with ER-mitochondria contact sites

Given that seipin deficiency alters mitochondrial properties, we investigated whether seipin is located at the ER-mitochondria contact sites, also known as mitochondria-associated membranes (MAMs). In A431 cells, using Airyscan imaging of fixed cells with endogenously GFP-tagged seipin, stably expressing mitochondria-targeted BFP and LipidTOX staining to visualize LDs, we observed that ~20% of seipin foci were localized juxtaposed to mitochondria, ~15% next to LDs, and ~10% juxtaposed to both (Figures 2A and 2B). The fraction of seipin overlapping with mitochondria decreased upon lipid loading with oleic acid, suggesting that the cellular localization of seipin is metabolically regulated (Figure 2C). When the localization of endogenously tagged seipin was studied using immunoelectron microscopy (immuno-EM), we found seipin labeling often at both ER-LD contact sites, as expected (Salo et al., 2016), and at ER-mitochondria contact sites (Figure 2D). Stereological analysis revealed a clear enrichment of seipin at MAMs (Figure 2E). We also performed immuno-EM analysis of previously reported seipin KO cell lines stably expressing low levels of WT- or BSCL2-associated A212P-seipin-GFP (Salo et al., 2016). WT-seipin was more enriched at MAMs than the BSCL-associated A212P-seipin (Figures S1A and S1B), supporting the notion that seipin localization at MAMs is functionally relevant.

We next assessed the relationship between seipin foci and mitochondria in A431 cells using live cell Airyscan imaging to simultaneously scan endogenously tagged seipin, mitochondria, and the ER. Whilst seipin was consistently associated with the ER, we found numerous examples wherein seipin foci appear to be transiently stabilized at sites juxtaposed to mitochondria (Figure 2F). Although most of the seipin-mitochondria interactions were short-lived (under 10 s) (Figure 2G), the mean motility of seipin foci at mitochondria was significantly decreased compared with seipin foci not associated with mitochondria (Figure 2H). These observations are in line with our imaging data from fixed cells, showing that a fraction of seipin specifically localizes at mitochondria-ER contact sites. However, we noted that seipin-mitochondria interactions are not as long lasting as seipin-LD interactions, which appear to be stable at least on the minute timescale (Salo et al., 2019, 2020).

To investigate whether seipin associates with mitochondria also in adipocytes, we performed subcellular fractionations of differentiated 3T3-L1 adipocytes expressing HA-tagged endogenous seipin. This cell line was generated by CRISPR-Cas9 gene editing and validated by western blotting, immunoprecipitation, and immunofluorescence (Figures S1C and S1D). Western blot analysis of subcellular fractions revealed

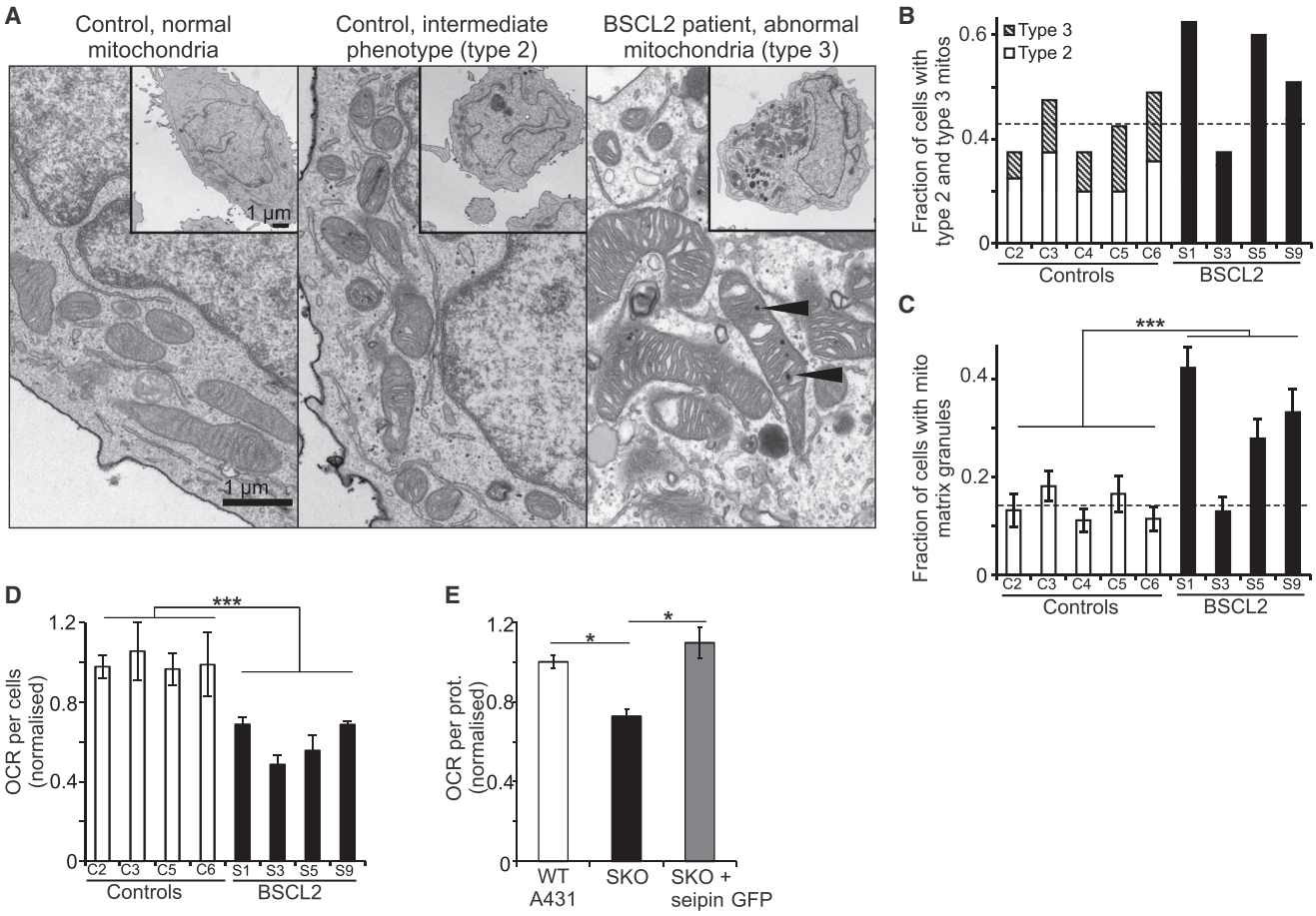

Figure 1. Mitochondria display abnormal morphology and reduced oxygen consumption in BSCL2 patients' cells

(A) TEM micrographs of control and BSCL2 patient lymphoblasts. Normal mitochondria: electron density similar to ER lumen, well-organized cristae (type 1). Abnormal mitochondria: dilated and disorganized cristae (type 3). Intermediate phenotype: some disorganization in a fraction of mitochondria (type 2). Arrowheads: matrix granules.

(B) Analysis of mitochondrial morphology in control and BSCL2 lymphoblasts from (A). Bars: percent of cells exhibiting type 2 and 3 mitochondria. n = 19–20 cells. The dashed line indicates the average of controls.

(C) Bars: percent of mitochondrial profiles with matrix granules ±SEM. n = 19–21 cells, 208–519 mitochondria. The dashed line indicates the average of controls. ***p < 0.005 Mann-Whitney test.

(D) Oxygen consumption rate analysis of control and BSCL2 lymphoblasts. Bars: mean ± SEM, n = 15–24 replicates/cells, 3 experiments. ***p < 0.005 Mann-Whitney test.

(E) OCR analysis of epidermoid carcinoma A431 cells, either WT, seipin knockout (SKO), or SKO stably expressing GFP-tagged seipin. Bars: average of basal OCR normalized to WT cells ± SEM. n = 30–45,*p < 0.05, Student's t test).

that, in 3T3-L1 adipocytes, seipin was present in the ER and MAM fractions, with a marked enrichment in the MAM fraction (Figure 2I).

To identify seipin-interacting proteins, we immunoprecipitated endogenous seipin from 3T3-L1 cells using HA antibodies and analyzed the products by mass spectrometry. The following criteria were used: a minimum of five peptides identified in the seipin-HA clone immunoprecipitation product and no peptide in the control clone precipitation (Table S1). The list of seipin-interacting proteins included SERCA2 and the inositol 3 phosphate receptor (IP3R), two ER proteins that localize to MAMs (Hayashi et al., 2009). Altogether, these data demonstrate that seipin is enriched at MAMs in both human A431 cells and murine adipocytes and interacts with the MAM proteins SERCA2 and IP3R.

Seipin interacts with SERCA2 and IP3R in MAMs and controls mitochondrial calcium import in A431 cells

In A431 cells, using proximity ligation assay (PLA), which allows quantitative analysis of *in situ* interactions at subcellular resolution (Salo et al., 2016), we detected specific signals for seipin/SERCA2 and seipin/IP3R proximity (Figures 3A and 3B). A substantial fraction (~40%) of PLA foci co-localized with mitochondrial staining (Figure 3C), suggesting that seipin may interact with SERCA2 and IP3R specifically at MAMs. Indeed, live cell Airyscan imaging of endogenously tagged IP3R and seipin in A431

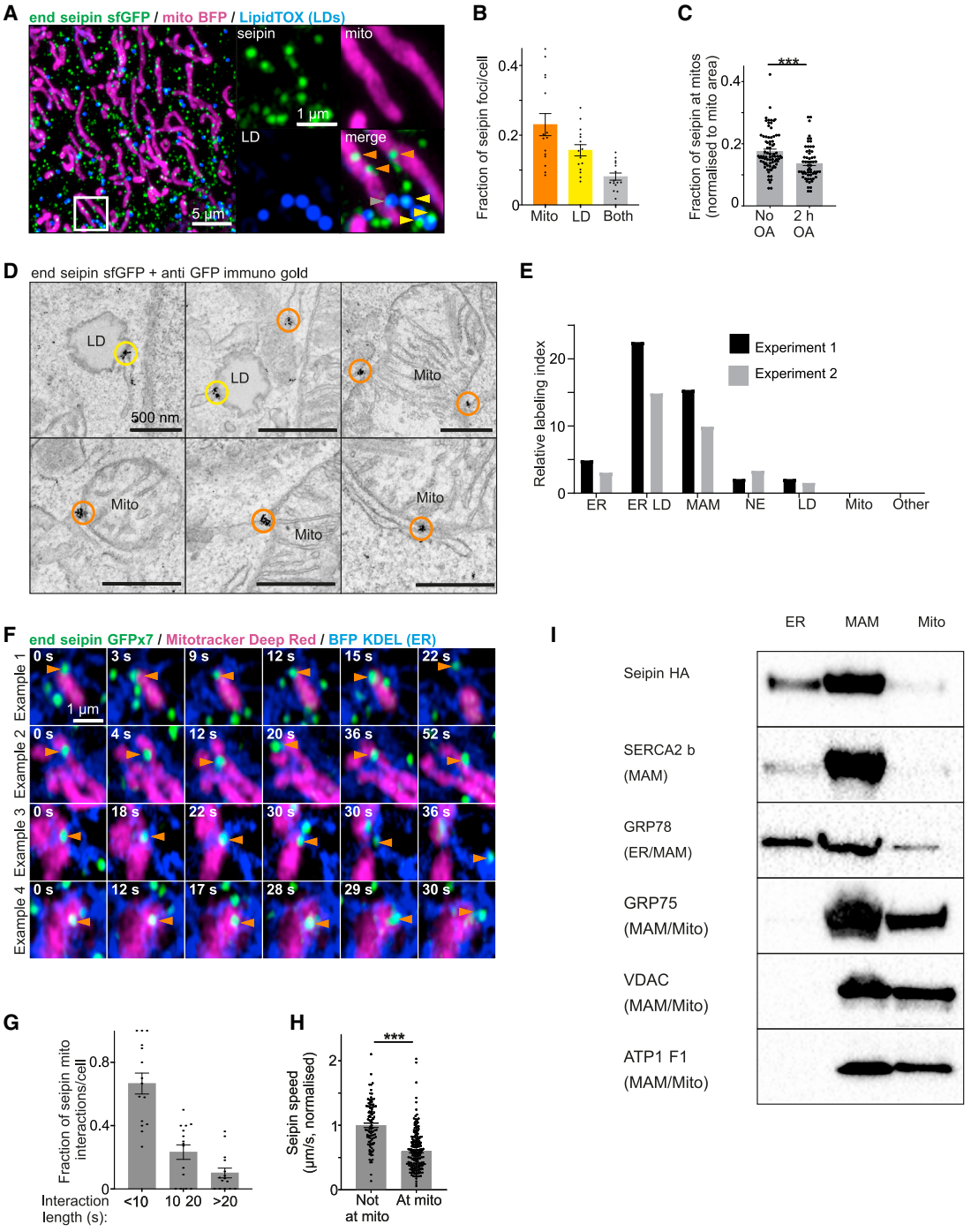

Figure 2. Seipin is associated with ER-mitochondria contact sites

(A) A431 cells with seipin tagged endogenously with sfGFP and stably expressing BFP-Mito were treated with oleic acid (OA) for 1 h, fixed, stained for LDs using LipidTOX Deep Red, and imaged using Airyscan microscopy. Maximum intensity of an Airyscan z stack. Orange, yellow, and gray arrowheads indicate seipin associated with mitochondria, LDs, or both, respectively.

(B) Analysis of (A). Bars: mean ± SEM. n = 15 cells, 2 experiments.

(C) A431 end-seipin-GFPx7 cells stably expressing BFP-Mito were treated or not with OA for 2 h, fixed, imaged by Airyscan microscopy, and seipin localization at mitochondria was analyzed. Bars: mean ± SEM, n = 59–78 cells, 3 experiments. ***p < 0.005 Mann-Whitney test.

(D) A431 end-seipin-sfGFP cells were immunolabeled for TEM with anti-GFP antibodies. Yellow circles: immunogold at ER-LD contacts; orange circles: immunogold at ER-mitochondria contacts.

(legend continued on next page)

cells revealed dynamic co-localization events at MAMs and also elsewhere in the cell (Figures S1E and S1G). Interestingly, seipin ablation resulted in reduced localization of IP3R at MAMs (Figure 3D) without obvious changes in IP3R protein levels (Figure S1H). Of note, a specific PLA signal was also obtained between seipin and voltage-dependent anion channel (VDAC1), a mitochondrial protein interacting with IP3R at MAMs and controlling ER/mitochondria Ca^{2+} exchange (Theurey and Rieusset, 2017) (Figure 3E).

As SERCA2, IP3R, and VDAC1 are key ER calcium (Ca^{2+}) store regulators, we investigated whether seipin deficiency alters Ca^{2+} handling. We utilized seipin degron cells, where seipin can be rapidly depleted upon administration of the plant hormone auxin (indole-acetic acid [IAA]), with >95% reduction in seipin protein content within 30 min (Salo et al., 2019) (Figure 3F). We transiently expressed cytosolic or mitochondrial targeted aequorin probes (Bonora et al., 2013) and measured the relative increase in cytosolic or mitochondrial Ca^{2+} in response to stimulation by ATP, histamine, and bradykinin. While IAA administration to control cells did not affect calcium flux into either compartment, acute seipin depletion decreased Ca^{2+} influx into the mitochondria, but not into the cytosol (Figures 3G and 3H). We also employed a parallel approach, using control or seipin degron cells stably expressing a mitochondrially targeted variant of the CEPIA calcium probe (Suzuki et al., 2014). Also with this strategy, mitochondrial calcium influx upon stimulus was decreased after acute depletion of seipin (Figures 3I and 3J). Moreover, ER Ca^{2+} stores were investigated by a complementary approach with the cytosolic calcium probe Fura2, measuring Ca^{2+} release into the cytosol upon SERCA2 inhibition with thapsigargin. In the presence of 1 mM extracellular Ca^{2+}, the cytosolic Ca^{2+} increase was not altered by seipin removal (Figures S2A and S2B). Altogether, these data provide evidence that, in A431 cells, seipin interacts with key MAM Ca^{2+} regulators in MAMs, and that acute seipin deletion impairs mitochondrial Ca^{2+} import.

Acute seipin deletion impairs mitochondrial calcium import and mitochondrial metabolism in 3T3L-1 adipocytes

We next examined the effects of 3 days of *BSCL2* silencing by siRNAs on Ca^{2+} handling in differentiated 3T3-L1 adipocytes (Figure 4A). We pre-treated the cells with caged-IP3 that can be photolyzed by a UV flash, thus specifically activating IP3R (Figure 4B). We monitored the effect of IP3 activation on cytosolic Ca^{2+} using Fluo4 and on mitochondrial Ca^{2+} using Rhod2. IP3 activation resulted in a higher cytosolic calcium response in siBSCL2-treated cells as compared with control (Figure 4C). In contrast, mitochondrial calcium import following IP3R activation was impaired in BSCL2 knockdown cells, suggesting that seipin is required for calcium exchange between the ER and mitochondria through IP3R (Figure 4D). Of note, at this time point of *BSCL2* silencing, expression of adipocyte markers such as adiponectin and PPARγ was not altered compared with control siRNA-treated adipocytes (Figures S2C and S2D). To study if this impairment in mitochondrial calcium import is due to an alteration in the ER calcium store, we performed experiments in Ca^{2+}-free medium avoiding the contribution of extracellular Ca^{2+}. Photolysis of caged-IP3 resulted in a similar cytosolic Ca^{2+} release in both conditions but, as in the previous experiment, the area under the curve was higher in siBSCL2 cells (Figure S2E). Treatment with thapsigargin, which prevents Ca^{2+} uptake into the ER, evoked a similar Ca^{2+} release in control cells and siBSCL2 cells, suggesting that seipin deficiency does not directly alter ER calcium stores (Figure S2E).

Finally, as Ca^{2+} is a key regulator of several mitochondrial enzyme activities, we analyzed whether seipin deficiency impairs mitochondrial function in 3T3-L1 adipocytes. No significant difference in OCR was observed between control and BSCL2 depleted cells (Figure 4E). However, an increase in extracellular acidification rate was found upon seipin depletion (Figure 4F). To further explore the metabolic consequences of seipin deficiency, we measured the levels of ATP, as well as several metabolites of glucose, including pyruvate, lactate, and intermediates of the tricarboxylic acid (TCA) cycle. BSCL2-depleted adipocytes show a significant decrease in ATP levels (Figure 4G). In addition, pyruvate was similar in both cells, but all the Krebs cycle metabolites were decreased in the absence of seipin (Figure 4H). Using ^{13}C-labeled glucose-based fluxomic analysis, we found that during a 3 h incubation, the production rate of all the TCA cycle intermediates measured was decreased in seipin-deficient adipocytes (Figure 4I). As the AMPk is an important player linking energy metabolism and Ca^{2+} (Herzig and Shaw, 2018), we tested if seipin deficiency was associated with altered AMPk activation. The effect of seipin knockdown was independent of AMPk activation, as assessed by the phosphorylation level of AMPk (Figure S2F). Altogether, these data suggest that seipin is required for calcium import into mitochondria impacting the activity of the TCA cycle and ATP concentration.

Seipin interacts with MAM calcium regulators in a nutritionally regulated manner in 3T3-L1 adipocytes

We next asked whether seipin proximity with the calcium-regulating proteins in MAMs is under nutritional control. As assessed by PLA in differentiated 3T3-L1 adipocytes, seipin proximity with

(E) Stereological analysis of (D). Bars: relative labeling index of seipin in different cellular compartments. n = 207–822 immunogold clusters and 912–2,703 grid points from 2 experiments.
(F) A431 end-seipin-GFPx7 cells stably expressing the ER marker BFP-KDEL were imaged live using Airyscan microscopy. Orange arrowheads: mitochondria-associated seipin.
(G) Analysis of (F). The lengths of seipin association with mitochondria were analyzed. Bars: mean ± SEM, n = 191 seipin trajectories from 15 cells, 2 experiments.
(H) Analysis of (F). The mean speed of seipin trajectories is plotted. Bars: mean ± SEM, n = 102–191 seipin trajectories from 15 cells, 2 experiments.
(I) Western blot analysis of ER-mitochondria-associated membranes (MAMs), and mitochondria (mito) fraction from seipin-HA 3T3-L1 cells, with 25 μg of protein from each fraction. The fidelity of subcellular fractionations was confirmed by immunoblotting against known markers, with MAM enrichment of the known MAM protein, the sarco/ER Ca^{2+} ATPase (SERCA2), pan-ER enrichment of the ER chaperone GRP78, and mitochondrial and MAM enrichment of GRP75, VDAC, and ATP1-F7.

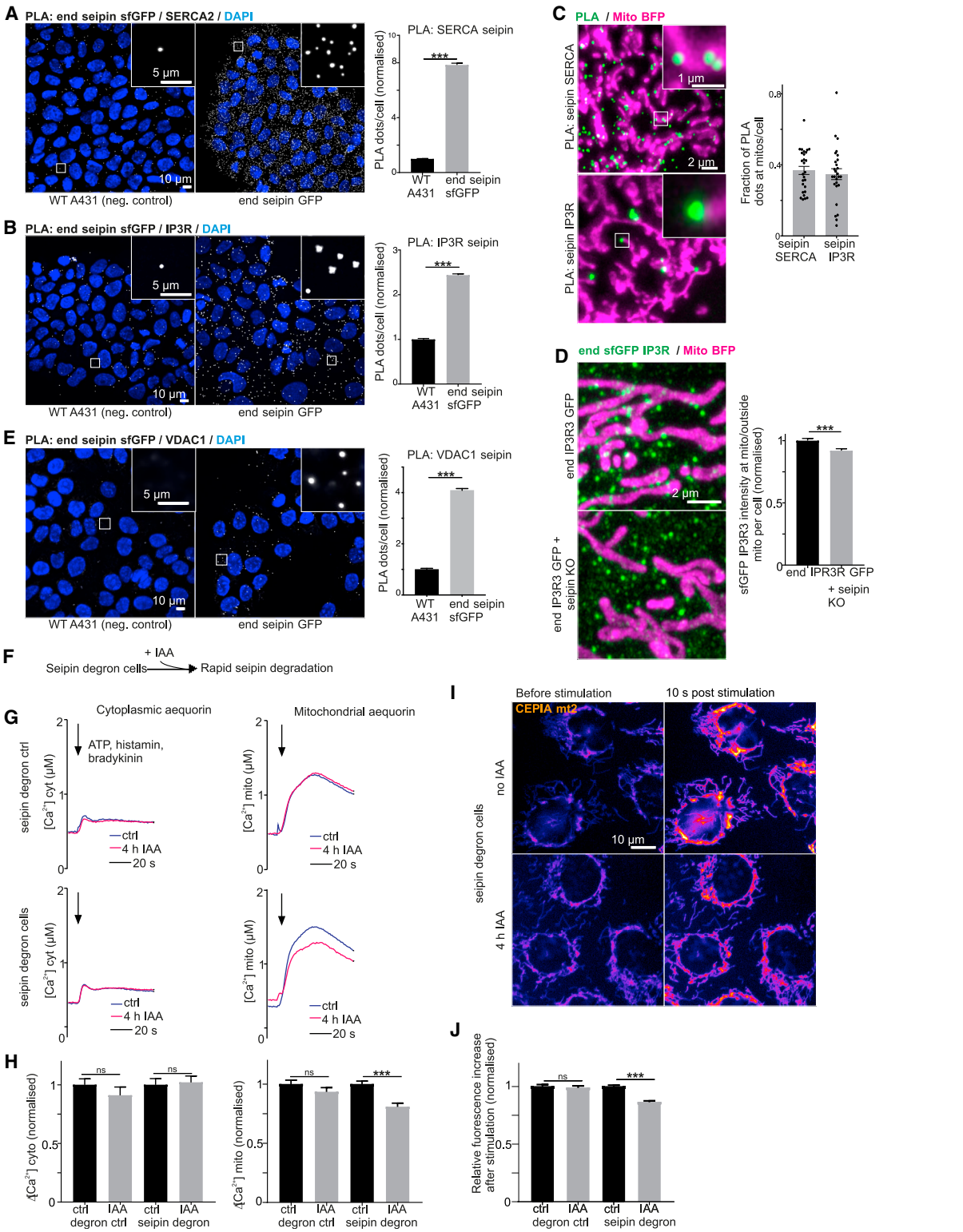

Figure 3. Seipin localizes close to SERCA2 and IP3R and its acute removal impairs mitochondrial calcium import in A431 cells

(A) Proximity ligation assay (PLA) was performed on fixed A431 WT and end-seipin-sfGFP cells with anti-GFP and anti-SERCA2 antibodies. Nuclei were stained with DAPI and cells were imaged using wide-field microscopy. Maximum intensity projections of deconvolved z stacks. Bars: mean ± SEM, n = >2,000 cells/group, 2 experiments. ***p < 0.005 Mann-Whitney test.

(legend continued on next page)

SERCA2 and IP3R was elevated in serum-starved conditions or with β3 agonist CL 316-243 treatment and decreased by oleic acid loading (Figures 5A, 5B, S3A, and S3B). Oleate loading also blunted seipin proximity with SERCA2 and IP3R in A431 cells (Figures S3G and S3H).

In line with the IP3R/seipin PLA results, seipin/VDAC proximity was elevated upon serum starvation or CL 316-243 treatment and reduced by oleate loading (Figures 5C and S3C). In contrast, oleate loading enhanced the proximity of seipin to the LD coat protein perilipin-1 and this signal was reduced upon starvation or CL316-243 treatment (Figures 5D and S3D). Finally, the nutritional inducers glucose and insulin reduced the proximity of seipin to VDAC as well as the proximity between VDAC and IP3R, which is classically used to quantify MAMs (Tubbs and Rieusset, 2016) (Figures 5E, 5F, S3E, and S3F). Together, these data support the idea that the localization of seipin in the vicinity of the MAM calcium regulatory proteins is promoted by starvation and reduced by ''fed-like'' conditions.

Inducible seipin removal from adipose tissue results in rapid mitochondrial dysfunction *in vivo*

In mice, total seipin KO leads to a nearly complete lack of fat (Prieur et al., 2013) and is therefore not a suitable model to explore seipin function in mature adipocytes *in vivo*. We thus generated Bscl2$^{lox/lox}$ mice × ERT2-Adipoq-CRE mice, allowing inducible seipin deletion in adipocytes upon tamoxifen addition (iATSKO). Indeed, a 5-day tamoxifen treatment led to a dramatic decrease in *Bscl2* mRNA in the adipose tissue (Figure S4A). This was accompanied by a decrease in inguinal fat pad weight from day 14 onward (Figure S4B). At day 90, iATSKO mice presented with a decreased body weight (Figure S4C), increased liver weight (Figure S4D), glucose intolerance (Figure S4E), and insulin resistance (Figure S4F). Histological analysis of inguinal adipose tissue revealed an abnormal morphology from day 14 onward and a decrease in adipocyte size at day 30 (Figures S4G and S4H). Paradoxically, at day 90 when the total fad pad was largely reduced (Figure S4B), the adipocyte size was increased (Figures S4G and S4H), suggesting that the remaining adipocytes became hypertrophic.

To study the effects of seipin deficiency *in vivo* on adipose tissue homeostasis in an unbiased manner, we used 3′-signal recognition particle RNA sequencing. This revealed 418 genes differentially expressed in inguinal adipose tissue of iATSKO mice compared with controls along the time course of 12 weeks upon *BSCL2* deletion (Figure 6A). Weighted correlation network analysis was used to identify clusters of genes that behaved similarly on the basis of their expression pattern. We identified six clusters of genes, among which clusters 1 and 2 drew our attention as, in these clusters, the iATSKO group stood out from the controls (Figures 6B and S5). We used gene ontology (GO) enrichment tools to identify the key pathways affected by the lack of seipin. Cluster 1 contains about 30 genes that were overexpressed in iATSKO mice as compared with controls, with one-third representing genes related to ER stress (Figure 6C). Cluster 2 was the largest group, about 200 genes, with reduced expression in iATSKO mice. These genes are connected to mitochondria function and the majority are involved in pyruvate metabolism or TCA cycle (Figure 6C). Multi-scale network analysis using MEGENA highlighted the existence of three more compact modules in cluster 2 (Figure 6D). The first sub-cluster contains genes encoding mitochondrial proteins involved in the respiratory chain, β-oxidation, or TCA cycle. The second sub-cluster contains genes linking TCA cycle products to lipogenesis: ATP citrate lyase (*Acly*) that catalyzes the conversion of citrate into acetyl-CoA, and fatty acid synthase (*Fas*) that catalyzes the synthesis of palmitate (C16) from acetyl-CoA and malonyl-CoA. GO analysis of the third sub-cluster did not reveal any major patterns. The decreased expression of TCA cycle and lipogenesis genes was confirmed by qPCR (Figures S6A–S6C). Of note, the expression levels of genes involved in catabolic processes, such as fatty acid oxidation (*Cpt1, PGC1a, Perilipin 5*) or thermogenesis (UCP1, Elovl3), were transiently increased at day 14 and then decreased at day 90 in iATSKO mice as compared with controls (Figures S6A–S6C).

To test whether the alterations in TCA cycle transcripts were associated with functional consequences, we measured the

(B) PLA was performed on fixed A431 WT and end-seipin-sfGFP cells with anti-GFP and anti-IP3R antibodies. Nuclei were stained with DAPI and cells were imaged using wide-field microscopy. Maximum intensity projections of deconvolved z stacks. Bars: mean ± SEM, n = >3,000 cells/group, 2 experiments. ***p < 0.005 Mann-Whitney test.
(C) PLA was performed on fixed end-seipin-sfGFP cells stably expressing mito-BFP with anti-GFP and anti-IP3R or SERCA2 antibodies. Maximum intensity projections of Airyscan z stacks. Bars: mean ± SEM. n = 27–32 cells, 2 experiments.
(D) A431 end-sfGFP-IP3R cells stably expressing mito-BFP with or without seipin KO were fixed and imaged using Airyscan microscopy. The mean intensity of end-sfGFP-IP3R overlapping with mitochondria or not was analyzed for each cell. Bars: mean ± SEM. n = 69–79 cells/group, 3 experiments. ***p < 0.005 Mann-Whitney test.
(E) PLA was performed on fixed A431 WT and end-seipin-sfGFP cells with anti-GFP and anti-VDAC1 antibodies. Nuclei were stained with DAPI and cells were imaged using wide-field microscopy. Maximum intensity projections of deconvolved z stacks. Bars: mean ± SEM. n = >3,000 cells/group, 2 experiments. ***p < 0.005 Mann-Whitney test.
(F) Schematic of seipin degron cells, wherein seipin can be inducibly depleted by addition of the small-molecule IAA.
(G) A431 seipin degron control and seipin degron cells were transfected with cytosolic or mitochondrially targeted luminescent Ca^{2+} indicator protein aequorin. Four hours after treatment with IAA, cells were stimulated as indicated and the increases in Ca^{2+} in the indicated compartments was recorded. Exemplary Ca^{2+} traces are shown.
(H) Analysis of (F). Bars: mean ± SEM. n = 17–34 wells/sample, 4 experiments. Ctrl indicates cells not treated with IAA. ***p < 0.005 Mann-Whitney test.
(I) A431 seipin degron control and seipin degron cells stably expressing the mitochondrially targeted fluorescent Ca^{2+} indicator protein CEPIA2mt were treated with IAA for 4 h and then stimulated as indicated. Single slices of wide-field images from live cells, representative images from seipin degron cells are shown.
(J) Analysis of (H). Bars: mean ± SEM. n = 416–1291 cells/sample, 3 experiments. Ctrl indicates cells not treated with IAA. ***p < 0.005 Mann-Whitney test.
For (G) and (I), data are normalized to each cell line without IAA addition within each experiment and data for seipin degron cells are pooled from two different clones.

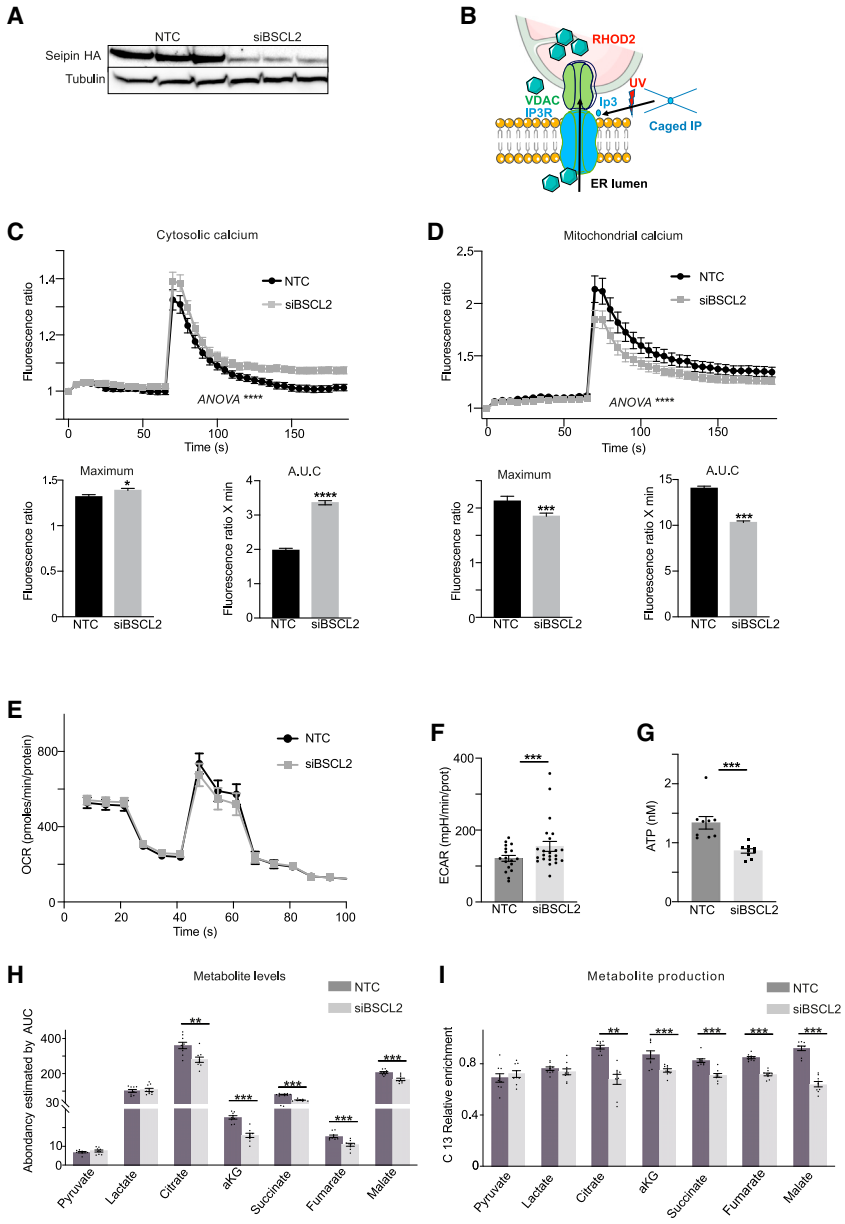

Figure 4. Reduced mitochondrial calcium import and TCA metabolite levels upon seipin depletion in 3T3-L1 adipocytes

(A) Immunoblot of S-HA 3T3-L1 cells treated with non-targeting control siRNA (NTC) or anti-Bscl2 siRNA (siBSCL2).

(B) Schematic of utilizing caged IP3 to measure intracellular calcium flux.

(C) 3T3-L1 cells treated with the indicated siRNAs were pre-incubated with caged IP3 and Fluo4 to monitor cytosolic calcium. After 60 s basal acquisition, flash UV-induced IP3 photolysis. The y axis represents the ratio over basal fluorescence. The area under the curve (AUC) was calculated with prism software and t test was performed on mean and standard deviation. Two-way ANOVA was performed on individual data points to assess if the fluorescence ratio was different over time between type of cells (NTC or siBSCL2). Bars: mean ± SEM. n > 120 cells/sample, 3 experiments.

(D) Cells were treated as analyzed as in (C), but using Rhod2 to monitor mitochondrial calcium. Bars: mean ± SEM. n > 120 cells/sample, 3 experiments.

(E and F) OCR and extracellular acidification rate (ECAR) were measured using the seahorse system. The area under the curve (AUC) was calculated with prism software and t test was performed on mean and standard deviation. Two-way ANOVA was performed on individual data points to assess if the fluorescence ratio was different over time between type of cells (NTC or siBSCL2). Bars: mean ± SEM, each condition in triplicate. n = 3 experiments.

(G) ATP concentration is evaluated by colorimetric assay.

(H and I) Total metabolites quantification and fractional enrichment of ^{13}C-glucose-derived glycolytic were analyzed by liquid chromatography-high-resolution mass spectrometry. aKG, α-ketoglutarate. Bars: mean ± SEM, each condition in triplicate. n = 3 experiments. ***p < 0.005 Mann-Whitney test.

levels of TCA cycle metabolites and ATP in inguinal fat pads. This demonstrated that citrate, succinate, and malate, as well as ATP levels, were all decreased in the adipose tissue of iATSKO mice already at 14 days after tamoxifen injection (Figure 7A). At 30 days, the ATP reduction had become more pronounced and the reduction in TCA cycle metabolites more widespread, with also fumarate levels decreased (Figure 7B).

In parallel, EM of inguinal adipose tissue revealed changes in mitochondrial morphology already at 14 days after the induction of *Bscl2* deletion. Mitochondria from iATSKO mouse adipocytes displayed decreased length and width as well as more prevalent constrictions, suggestive of increased mitochondrial fragmentation (Figures 7C–7F). As AMPk is known to regulate mitochondrial fission/fusion and ATP production (Herzig and Shaw, 2018), we analyzed its phosphorylation levels. Similarly, as in 3T3-L1 cells, seipin deficiency was not associated with altered AMPk activity (Figure S6D).

Finally, we analyzed if seipin deletion affected the compartmentalization of the MAM calcium regulators *in vivo*. To this end, we carried out subcellular fractionations of inguinal adipose tissue isolated from iATSKO and control mice at 14 days followed by western blotting. This demonstrated that, upon adipocyte seipin deficiency, SERCA2 became depleted in the MAM-enriched mitochondrial fraction but remained unchanged in the ER fraction and in the total lysate (Figure 7G). Together, these findings strongly suggest that the lack of seipin rapidly and profoundly affects mitochondrial properties in mouse adipose tissue.

DISCUSSION

Here, we demonstrate that seipin is enriched at ER-mitochondria contact sites, also called MAMs. We found that seipin interacted

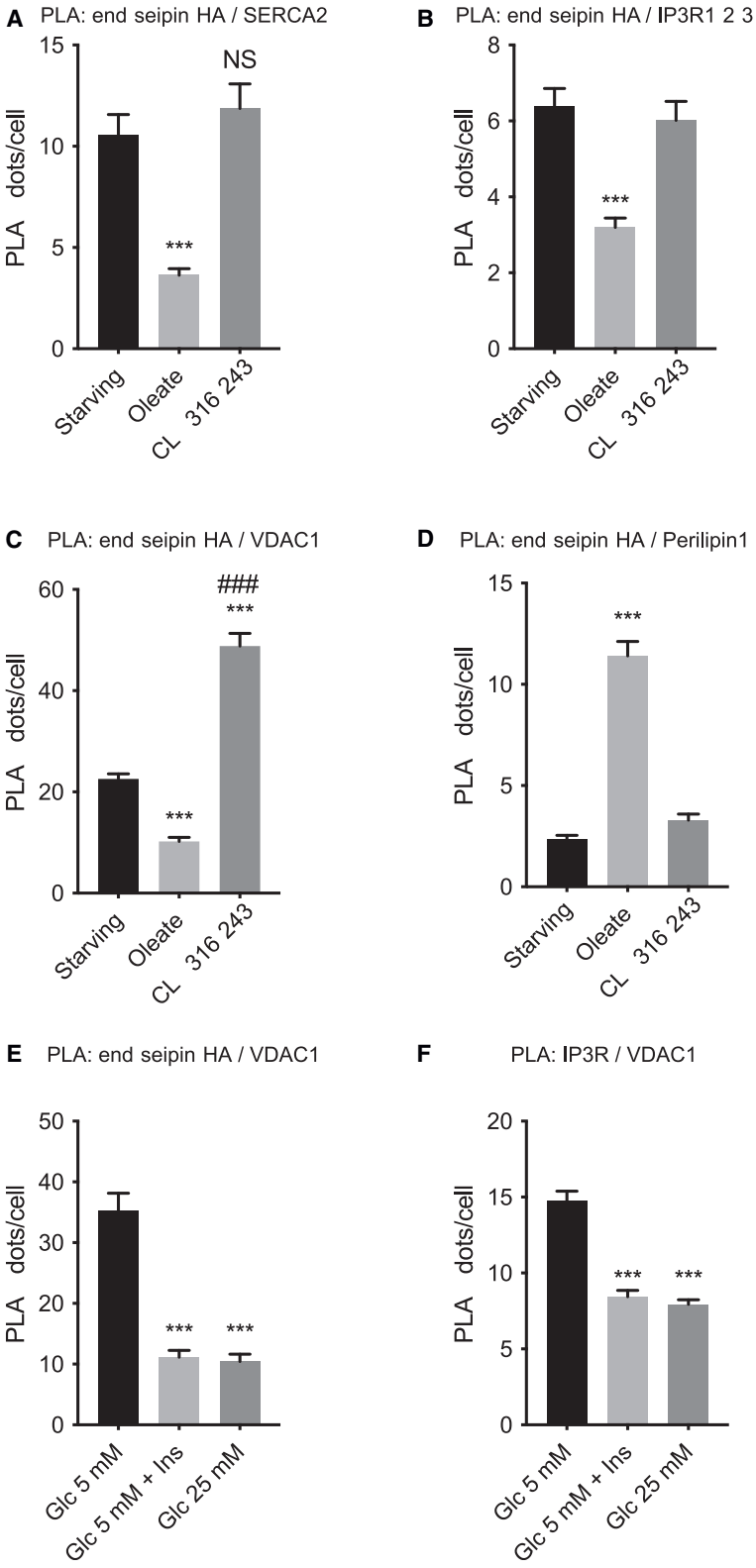

Figure 5. The interaction of seipin with SERCA2 and IP3R is nutritionally regulated in 3T3-L1 adipocytes

(A–D) PLA reaction was performed on fixed S-HA 3T3-L1cells with anti-HA (recognizing endogenously tagged seipin) and anti-SERCA2 (A), anti-IP3R (B), anti-VDAC1 (C), or anti-Perilipin1 (D) antibodies. Cells were maintained in serum-starved conditions, with 700 μM oleate or 5 μM CL316-243 as indicated, for 6 h. Bars: mean ± SEM. n > 1,500 cells, 2 experiments.

(E and F) PLA reaction was performed on fixed S-HA 3T3-L1 cells with anti-HA (recognizing endogenously tagged seipin) and anti-VDAC antibodies (E) or anti-IP3R and anti-VDAC1 antibodies (F). Cells were maintained in serum-starved conditions containing glucose and insulin as indicated. Bars: mean ± SEM. n > 1,500 cells/2 experiments. For all panels, bars: mean ± SEM. ns indicates $p > 0.05$, *$p < 0.05$, **$p < 0.01$, ***$p < 0.005$, as compared with starving condition, ###$p < 0.0001$ as compared with oleate condition, Student's t test.

with MAM-enriched proteins critical for ER calcium homeostasis: SERCA2, which transports cytosolic calcium into the ER lumen; and IP3R, which transports calcium from the ER via VDAC into the mitochondria. When seipin was acutely removed by auxin-inducible degradation, mitochondrial calcium import decreased within a few hours. The acuteness of this effect strongly suggests that the involvement of seipin in ER-to-mitochondria calcium flux is rather direct. Moreover, it is not readily compensated for, as in 3 days of seipin silencing, when adipocyte markers (adiponectin, PPARγ) were not altered, mitochondrial calcium influx upon IP3R activation was reduced. This was accompanied by a widespread reduction in Krebs cycle metabolites and ATP concentration. The activities of three TCA cycle enzymes, i.e., pyruvate dehydrogenase, α-ketoglutarate dehydrogenase, and isocitrate dehydrogenase, are calcium dependent (Denton, 2009), as possibly is ATP synthase (Williams et al., 2015). Moreover, mitochondrial calcium regulates the inner mitochondrial membrane potential that controls ATP synthase (Wescott et al., 2019). Thus, seipin at ER-mitochondrial contact sites appears to control mitochondrial calcium influx and this in turn affects the efficiency of the TCA cycle and ATP production.

The dynamic regulation of MAMs by nutrient availability is only starting to emerge. In the liver, starvation increased the extent of MAMs, promoting mitochondrial fusion, calcium import, and ATP production, while a fed state reduced MAMs and mitochondrial activity (Theurey et al., 2016). Our observation that starvation increased the proximity of IP3R and VDAC, an indicator of MAMs (Tubbs and Rieusset, 2016), suggests that such a regulation may also apply for adipocytes. Moreover, if seipin affects mitochondrial energy supply via MAM-associated calcium regulators, one might expect this to be nutritionally regulated. Indeed, we found that, in adipocytes, endogenous seipin favored proximity to SERCA and IP3R under starvation conditions as compared with oleate loading, when seipin was increasingly in the vicinity of the LD protein perilipin. The latter agrees with the recruitment

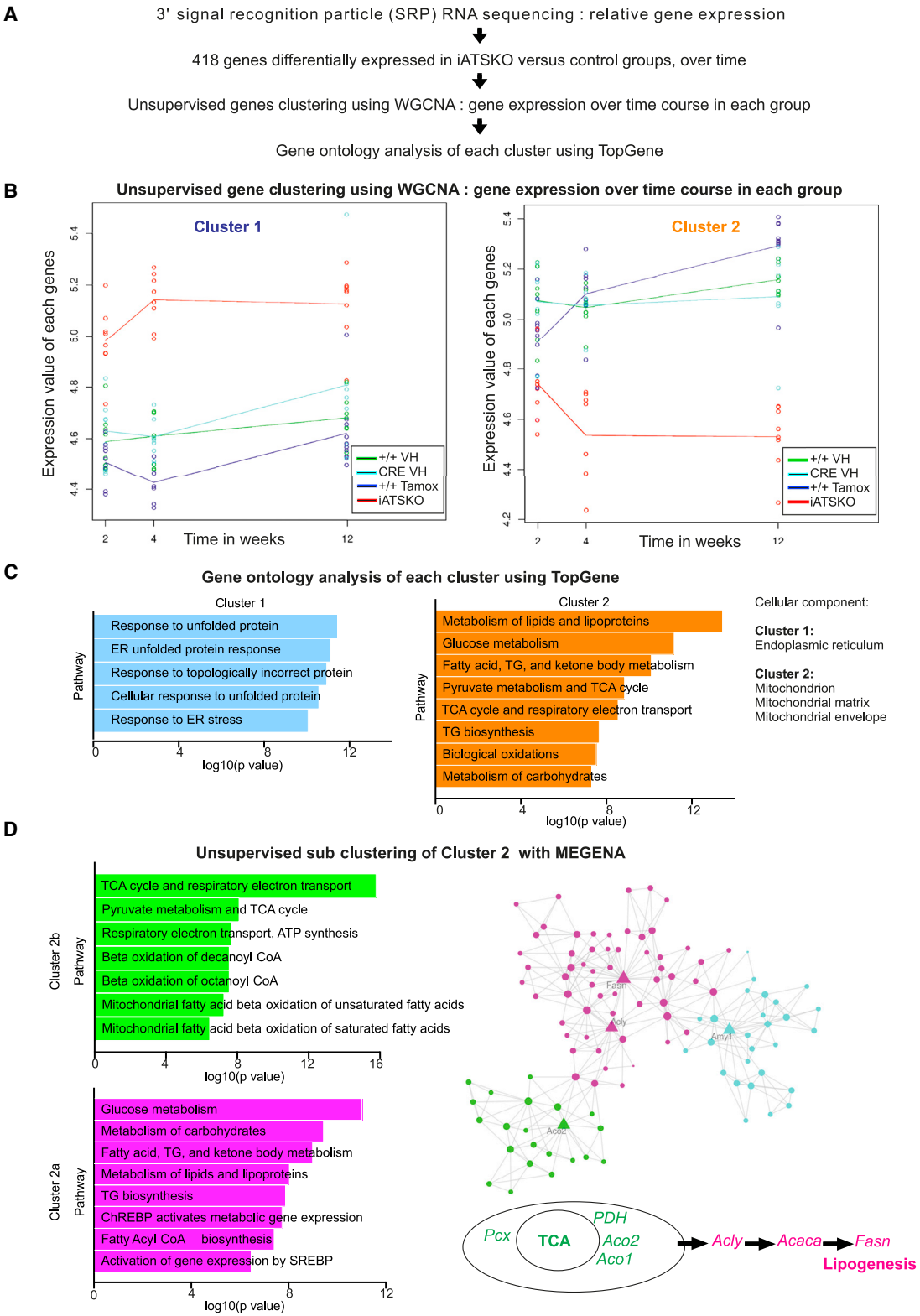

(legend on next page)

of seipin to ER-LD contacts upon oleate loading in other cell types (Salo et al., 2016, 2019; Wang et al., 2016). We also noted that stimuli mimicking fasting conditions (starvation, low glucose, and β3 agonist treatment) promoted the proximity of seipin to VDAC, while fed-like stimuli (lipids, glucose, insulin) reduced it. These results suggest that seipin exerts different biological functions according to the metabolic status, by facilitating lipid deposition from ER to LDs under lipid loading conditions and calcium flux from ER-to-mitochondria under starvation. We speculate that seipin controls mitochondrial calcium influx by compartmentalizing MAM calcium regulators, as seipin deficiency reduced IP3R and SERCA2 enrichment at MAMs.

Work by the Huang lab first demonstrated that, in *Drosophila*, seipin interacts with SERCA (Bi et al., 2014). They reported that dSeipin regulates ER calcium stores by interacting with SERCA and that, in dSeipin mutants, the decrease in ER calcium store can be partially rescued by knocking down the ER-to-cytosol calcium release channel ryanodine receptor (RyR) (Bi et al., 2014). RyR knockdown also partially restored fat storage in the mutant flies. The ER calcium reduction in dSeipin mutants resulted in decreased mitochondrial calcium, thereby compromising the production of citrate and acetyl-CoA (Ding et al., 2018). Furthermore, they proposed that a dramatic reduction of citrate (to less than 10% of normal levels) is a critical missing component for lipogenesis in dSeipin mutants. In support of this, citrate supplementation rescued the lipid storage defect in dSeipin mutant fat cells (Ding et al., 2018).

The role of seipin in ER calcium homeostasis appears to differ between *Drosophila* and the two mammalian seipin-deficient systems studied here, A431 cells and adipocytes. First, in these cells, seipin deficiency was not accompanied by alterations in ER calcium stores. Second, we found seipin to interact with IP3R and to regulate IP3R-controlled mitochondrial calcium influx. Third, we observed a moderate and widespread reduction of TCA cycle metabolites in seipin-deficient mouse adipocytes. However, citrate failed to rescue the lipid storage defect in seipin-deficient human cells (Figures S7A and S7B). We also tested the effect of the potent RyR agonist caffeine in 3T3-L1 adipocytes but did not find any effects on ER calcium efflux, suggesting that RyR is not the main exit route for ER calcium in adipocytes (Figure S7C). Interestingly, a caffeine-induced Ca^{2+} transport dysfunction was recently reported in seipin-deficient cardiomyocytes (Wu et al., 2021), speaking for cell type differences in ER calcium homeostasis.

Of note, besides species-/cell-type differences, some of the alterations may be due to differences in the timing of events. Our experiments were carried out under acute seipin depletion (hours to days), whereas the earlier results are from a constitutive dSeipin mutant system. For instance, the reduced ER calcium store might develop over time, with reduced ATP levels contributing to reduced SERCA ATPase activity. The differences between our two models might also be related to the acuteness of seipin depletion. In A431 cells we did not observe any effect on cytosolic calcium response upon 4 h of seipin removal. However, cytosolic calcium was modestly but significantly increased after ER calcium release in 3T3-L1 cells where seipin had been silenced for 3 days. This could be a late effect of seipin knockdown.

The characterization of the inducible adipose tissue seipin knockout mouse model allowed us to reveal mitochondrial dysfunction as an early sign of seipin depletion from mature adipocytes. This included widespread changes in transcripts encoding mitochondrial processes, decreased TCA cycle metabolites, reduced ATP concentration, and mitochondrial fragmentation, in line with the notion that fragmented mitochondria produce less ATP (Gao et al., 2014). Interestingly, we also observed a transient induction of fatty acid oxidation and thermogenic genes at 14 days of seipin removal. This agrees with the findings of Zhou et al. (2015) reporting increased transcripts of thermogenic and β-oxidation genes at 10 days upon seipin deletion in a similar mouse model. Considering the reduced ATP levels detected in our experiments, we hypothesize that, upon seipin deficiency, the ensuing mitochondrial dysfunction promotes uncoupling and prevents lipid catabolism from producing ATP. The progressive loss of adipose tissue observed at later times may result, at least in part, from the severely reduced ATP levels (50% decrease at 30 days of seipin removal), which may compromise adipocyte properties and finally cell survival, as reported previously (Kusminski and Scherer, 2012). Importantly, the mitochondrial changes are long lasting and not limited to adipocytes, as dysfunctional mitochondria are also characteristic to BSCL2 patient cells.

In summary, this study shows that mammalian seipin is localized at ER-mitochondrial contacts and associates with ER-mitochondrial calcium regulators IP3R and VDAC in a nutrition-dependent manner, controlling mitochondrial calcium influx and energy supply in adipocytes. Further studies are needed to decipher how mitochondrial calcium influx is nutritionally regulated in adipocytes and how this contributes to regulate mitochondria physiology and hence metabolic flexibility in this cell type.

Limitations of the study

The present work demonstrates that seipin deficiency impairs ER-to-mitochondria calcium import and alters mitochondrial properties in A431 cells and adipocytes. In mice, we show that seipin deficiency also alters mitochondrial properties but cannot demonstrate an alteration of ER-mitochondria calcium import. To our knowledge, such tools to study calcium flux *in vivo*, *ex vivo*, or even in primary adipocytes are not readily available.

Figure 6. RNA sequencing analysis of seipin-deficient inguinal adipose tissue reveals acute mitochondrial dysfunction

(A) Schematic of data analysis pipeline.

(B) Weighted correlation network analysis (WGCNA) was used to identify clusters of genes that behave similarly on the basis of their expression pattern over time. The graphics represent the median expression of the genes and their pathways identified with TopGene for cluster 1 and cluster 2. The x axis indicates time after tamoxifen injection.

(C) Gene ontology analysis of the cluster using TopGene.

(D) MEGENA representation of the cluster 2-like and the associated pathway information.

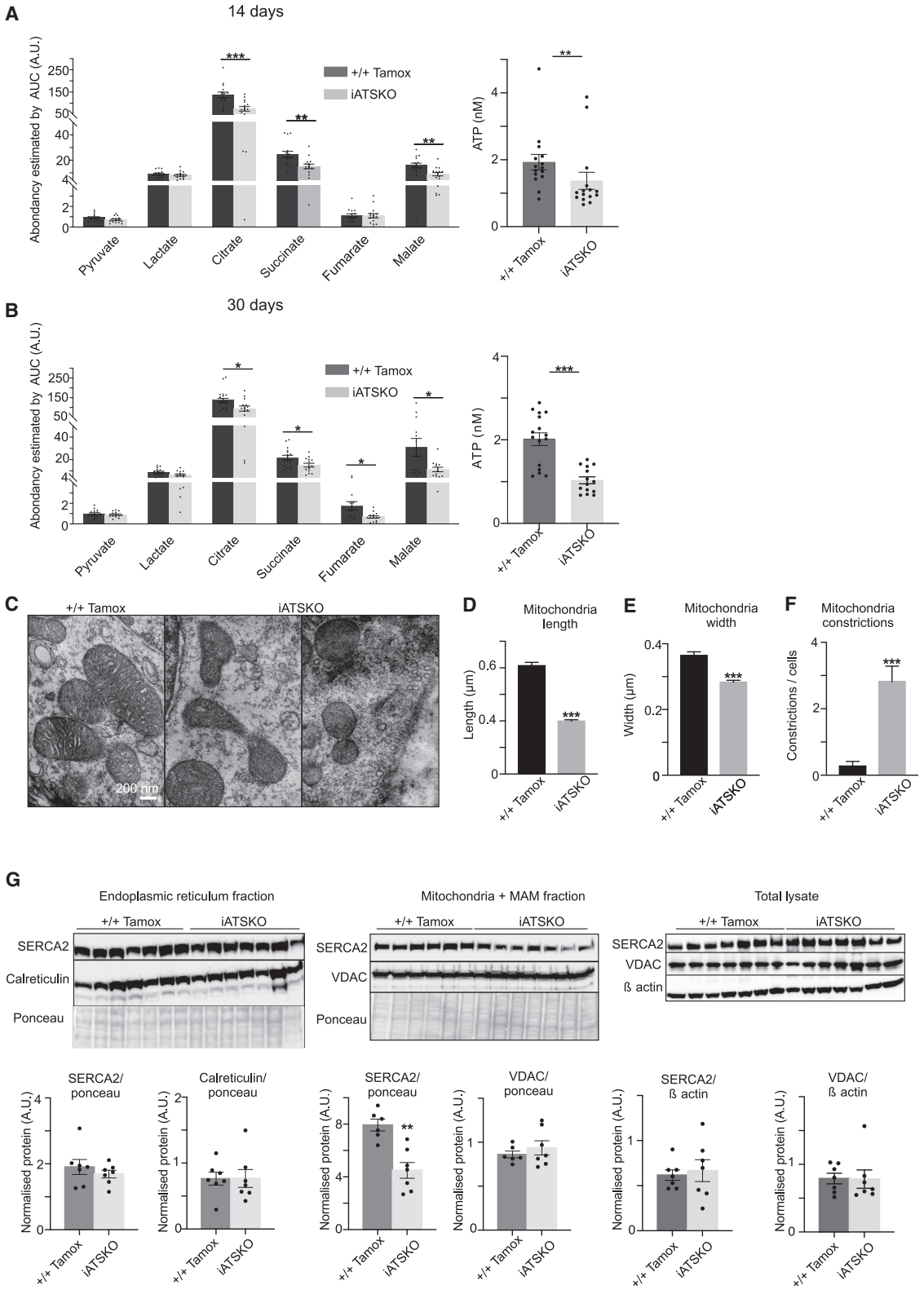

(legend on next page)

Therefore, evidence for a direct involvement of seipin in calcium handling *in vivo* is currently lacking. In addition, we provide evidence that seipin deficiency decreases SERCA2 enrichment in MAMs *in vivo*, but do not address whether seipin depletion affects the abundance or properties of MAMs more broadly. Indeed, the study of MAMs in adipose tissue is quite challenging, both by morphological techniques such as EM and by biochemical strategies, such as fractionation.

Our findings also raise questions on the role of seipin in MAMs in non-adipocyte cells, especially in tissues where seipin is suspected to play a cell autonomous function. For instance, it would be interesting to study seipin function in MAM and calcium exchange in pancreatic β cells, where calcium handling plays a central role and heterozygous seipin deletion (Xiong et al., 2020) is sufficient to impair glucose-stimulated insulin secretion. Finally, this study leaves open whether the seipin-regulated mitochondrial calcium import described here is functionally connected to the known role of seipin in LD formation. In this context it is interesting to note that lipid droplets can be generated under starvation conditions in close proximity to mitochondria, to protect from free fatty acid-induced lipotoxicity (Nguyen et al., 2017).

STAR★METHODS

Detailed methods are provided in the online version of this paper and include the following:

- KEY RESOURCES TABLE
- RESOURCE AVAILABILITY
  - Lead contact
  - Materials availability
  - Data and code availability
- EXPERIMENTAL MODEL AND SUBJECT DETAILS
  - Cell culture: A431 cells, lymphoblasts, and 3T3-L1 adipocytes
  - Stable A431 cell lines
  - Construction of end-sfGFP-IP3R cells
  - Generation of end-seipin-HA cells in 3T3L1-cells
  - Animals
- METHODS DETAILS
  - Subcellular fractionation and immunoblotting
  - PLA, immunofluorescence and LD analysis in A431 cells
  - PLA in 3T3-L1 cells
  - Live and fixed cell Airyscan microscopy and analysis
  - Calcium measurements
  - Mitochondrial metabolite quantification
  - 3'seq-RNA profiling
  - RNA analysis
  - OCR measurements in lymphoblasts
  - Immuno-electron microscopy
  - Transmission electron microscopy
  - Proteomic analysis
- QUANTIFICATION AND STATISTICAL ANALYSIS
  - Analysis of 3'seq-RNA profiling
  - Statistical analysis

SUPPLEMENTAL INFORMATION

Supplemental information can be found online at https://doi.org/10.1016/j.celrep.2021.110213.

ACKNOWLEDGMENTS

This study has been granted from Société Francophone du Diabète and the FFRD (sponsored by Fédération Française des Diabétiques, Abbott, AstraZeneca, Eli Lilly, Merck Sharp & Dohme, and Novo Nordisk) and the French National Research Agency (ANR-21-CE14-0024 MAMA). E.I. acknowledges support from the Academy of Finland (grants 307415 and 324929), University of Helsinki/HiLIFE Fellowship, Sigrid Jusélius Foundation, Jane and Aatos Erkko Foundation, and Fondation Leducq (grant 19CVD04). E.J. acknowledges support from the Academy of Finland (grant 1331998). Y.C. is funded by the Ministère de l'Enseignement Supérieur et de la Recherche. We thank Biocenter Finland and HiLIFE light microscopy, electron microscopy, and flow cytometry units. V.T.S. acknowledges support from the Finnish Medical, Paulo, Alfred Kordelin, Maud Kuistila, Biomedicum Helsinki, and Emil Aaltonen Foundation. We acknowledge the MicroPICell facility, SFR Santé, INSERM, CNRS, UNIV Nantes, CHU Nantes, Nantes, France, member of the national infrastructure France-BioImaging supported by the French National Research Agency (ANR-10-INBS-04). We are most grateful to the Genomics and Bioinformatics Core Facility of Nantes (GenoBiRD, Biogenouest, IFB) for its technical support. We thank the Institut Clinique de la Souris—PHENOMIN for establishment of the Bscl2 Lox Lox mouse mutant line. We thank Pr Offermanns (Max Plank InstituteBad Nauheim, Germany) for the generous gift of the ERT2-Adipoq-CRE mice. We thank Evangéline Bennana, Cédric Broussard, and François Guillonneau from the 3P5 proteom'IC facility, Université de Paris, Institut Cochin, INSERM, CNRS, F-75014 PARIS, France. The Orbitrap Fusion mass spectrometer was acquired with funds from the FEDER through the "Operational Program for Competitiveness Factors and employment 2007-2013" and from the "Cancéropôle Ile-de-France."

AUTHOR CONTRIBUTIONS

V.T.S., M.H., K.V., and S.L. designed and performed experiments in A431 cells. B.L. and L.K. performed immuno-EM. Y.C. and G.C. designed and performed experiments in 3T3-L1 cells. J.R. and Y.C. set up the PLA in 3T3-L1 cells. Y.C. and S.D. performed the experiments in iATSKO mice. S.L.L. performed the EM on adipose tissue. C.L.M. and B.C. contributed to iATSKO experiment design. H.L. performed the bio-informatic analysis of

Figure 7. Seipin deficiency alters mitochondrial properties in mouse adipose tissue

(A and B) Metabolites levels and ATP concentration were evaluated in inguinal fat pad of Bscl2$^{lox/lox}$ tamoxifen (+/+ Tamox, in black) and iATSKO (gray) males, at 14 days (A) and 30 days (B) after tamoxifen injection. For all panels, bars: mean ± SEM. n = 8–11 for each group. *p < 0.05, **p < 0.01, ***p < 0.005, Mann-Whitney test.

(C–F) Mitochondrial morphology in inguinal adipose tissue from mice 14 days after tamoxifen injection was analyzed by EM. Bars: mean ± SEM. n = 4 mice per group, 5 cells per mice. ***p < 0.005 Student's t test.

(G) Western blot analysis of ER or crude mitochondrial fraction (25 μg of protein from each) isolated from inguinal adipose tissue from Bscl2$^{lox/lox}$ tamoxifen (+/+ Tamox) and Bscl2$^{lox/lox}$-RT2-Adipoq-CRE tamoxifen (iATSKO) males, at 14 days after tamoxifen injection. Total lysates were analyzed in parallel to assess the expression levels of SERCA2 and VDAC. Bars: mean ± SEM. n = 6–7, **p < 0.01 Mann-Whitney test.

transcriptomic data. H.V., I.B., and E.J. performed and analyzed EM experiments in A431 cells and lymphoblasts. C.P., M.C., and O.R. generated the metabolite measurement data. C.V. and J.M. generated the patient cell lines. I.P. and K.T. performed aequorin and Fura 2AM measurements in A431 cells. E.I. and X.P. supervised the project. E.I. and X.P. wrote the paper, and all authors commented on the paper. E.I. is the corresponding author for the A431 cells part of the paper. X.P. is the corresponding author for the adipocytes and mice part of the paper.

DECLARATION OF INTERESTS

The authors declare no competing interests.

Received: June 11, 2021
Revised: October 11, 2021
Accepted: December 14, 2021
Published: January 11, 2022

REFERENCES

Arruda, A.P., Pers, B.M., Parlakgul, G., Guney, E., Inouye, K., and Hotamisligil, G.S. (2014). Chronic enrichment of hepatic endoplasmic reticulum-mitochondria contact leads to mitochondrial dysfunction in obesity. Nat. Med. *20*, 1427–1435. https://doi.org/10.1038/nm.3735.

Belevich, I., Joensuu, M., Kumar, D., Vihinen, H., and Jokitalo, E. (2016). Microscopy image browser: a platform for segmentation and analysis of multidimensional datasets. PLoS Biol. *14*, e1002340. https://doi.org/10.1371/journal.pbio.1002340.

Benjamini, Y., and Hochberg, Y. (1995). Controlling the false discovery rate: a practical and powerful approach to multiple testing. J. R. Stat. Soc. Ser. B, 289–300.

Berg, S., Kutra, D., Kroeger, T., Straehle, C.N., Kausler, B.X., Haubold, C., Schiegg, M., Ales, J., Beier, T., Rudy, M., et al. (2019). ilastik: interactive machine learning for (bio)image analysis. Nat. Methods *16*, 1226–1232. https://doi.org/10.1038/s41592-019-0582-9.

Bi, J., Wang, W., Liu, Z., Huang, X., Jiang, Q., Liu, G., Wang, Y., and Huang, X. (2014). Seipin promotes adipose tissue fat storage through the ER Ca(2)(+)-ATPase SERCA. Cell Metab. *19*, 861–871. https://doi.org/10.1016/j.cmet.2014.03.028.

Birling, M.C., Dierich, A., Jacquot, S., Herault, Y., and Pavlovic, G. (2012). Highly-efficient, fluorescent, locus directed cre and FlpO deleter mice on a pure C57BL/6N genetic background. Genesis *50*, 482–489. https://doi.org/10.1002/dvg.20826.

Bonora, M., Giorgi, C., Bononi, A., Marchi, S., Patergnani, S., Rimessi, A., Rizzuto, R., and Pinton, P. (2013). Subcellular calcium measurements in mammalian cells using jellyfish photoprotein aequorin-based probes. Nat. Protoc. *8*, 2105–2118. https://doi.org/10.1038/nprot.2013.127.

Boutet, E., El Mourabit, H., Prot, M., Nemani, M., Khallouf, E., Colard, O., Maurice, M., Durand-Schneider, A.M., Chretien, Y., Gres, S., et al. (2009). Seipin deficiency alters fatty acid Delta9 desaturation and lipid droplet formation in Berardinelli-Seip congenital lipodystrophy. Biochimie *91*, 796–803. https://doi.org/10.1016/j.biochi.2009.01.011.

Cacchiarelli, D., Trapnell, C., Ziller, M.J., Soumillon, M., Cesana, M., Karnik, R., Donaghey, J., Smith, Z.D., Ratanasirintrawoot, S., Zhang, X., et al. (2015). Integrative analyses of human reprogramming reveal dynamic nature of induced pluripotency. Cell *162*, 412–424. https://doi.org/10.1016/j.cell.2015.06.016.

Carpenter, A.E., Jones, T.R., Lamprecht, M.R., Clarke, C., Kang, I.H., Friman, O., Guertin, D.A., Chang, J.H., Lindquist, R.A., Moffat, J., et al. (2006). CellProfiler: image analysis software for identifying and quantifying cell phenotypes. Genome Biol. *7*, R100. https://doi.org/10.1186/gb-2006-7-10-r100.

Chen, W., Chang, B., Saha, P., Hartig, S.M., Li, L., Reddy, V.T., Yang, Y., Yechoor, V., Mancini, M.A., and Chan, L. (2012). Berardinelli-Seip congenital lipodystrophy 2/seipin is a cell-autonomous regulator of lipolysis essential for adipocyte differentiation. Mol. Cell Biol. *32*, 1099–1111. https://doi.org/10.1128/MCB.06465-11.

Cheyette, T.E., and Gross, D.J. (1991). Epidermal growth factor-stimulated calcium ion transients in individual A431 cells: initiation kinetics and ligand concentration dependence. Cell Regul. *2*, 827–840. https://doi.org/10.1091/mbc.2.10.827.

Conesa, A., Nueda, M.J., Ferrer, A., and Talon, M. (2006). maSigPro: a method to identify significantly differential expression profiles in time-course microarray experiments. Bioinformatics *22*, 1096–1102. https://doi.org/10.1093/bioinformatics/btl056.

Cui, X., Wang, Y., Tang, Y., Liu, Y., Zhao, L., Deng, J., Xu, G., Peng, X., Ju, S., Liu, G., and Yang, H. (2011). Seipin ablation in mice results in severe generalized lipodystrophy. Hum. Mol. Genet. *20*, 3022–3030. https://doi.org/10.1093/hmg/ddr205.

Denton, R.M. (2009). Regulation of mitochondrial dehydrogenases by calcium ions. Biochim. Biophys. Acta *1787*, 1309–1316. https://doi.org/10.1016/j.bbabio.2009.01.005.

Ding, L., Yang, X., Tian, H., Liang, J., Zhang, F., Wang, G., Wang, Y., Ding, M., Shui, G., and Huang, X. (2018). Seipin regulates lipid homeostasis by ensuring calcium-dependent mitochondrial metabolism. EMBO J. *37*. https://doi.org/10.15252/embj.201797572.

Dollet, L., Magre, J., Joubert, M., Le May, C., Ayer, A., Arnaud, L., Pecqueur, C., Blouin, V., Cariou, B., and Prieur, X. (2016). Seipin deficiency alters brown adipose tissue thermogenesis and insulin sensitivity in a non-cell autonomous mode. Sci. Rep. *6*, 35487. https://doi.org/10.1038/srep35487.

Fei, W., Shui, G., Gaeta, B., Du, X., Kuerschner, L., Li, P., Brown, A.J., Wenk, M.R., Parton, R.G., and Yang, H. (2008). Fld1p, a functional homologue of human seipin, regulates the size of lipid droplets in yeast. J. Cell Biol. *180*, 473–482. https://doi.org/10.1083/jcb.200711136.

Fei, W., Shui, G., Zhang, Y., Krahmer, N., Ferguson, C., Kapterian, T.S., Lin, R.C., Dawes, I.W., Brown, A.J., Li, P., et al. (2011). A role for phosphatidic acid in the formation of "supersized" lipid droplets. PLoS Genet *7*, e1002201. https://doi.org/10.1371/journal.pgen.1002201.

Friedman, J.R., Lackner, L.L., West, M., DiBenedetto, J.R., Nunnari, J., and Voeltz, G.K. (2011). ER tubules mark sites of mitochondrial division. Science *334*, 358–362. https://doi.org/10.1126/science.1207385.

Fu, S., Yang, L., Li, P., Hofmann, O., Dicker, L., Hide, W., Lin, X., Watkins, S.M., Ivanov, A.R., and Hotamisligil, G.S. (2011). Aberrant lipid metabolism disrupts calcium homeostasis causing liver endoplasmic reticulum stress in obesity. Nature *473*, 528–531. https://doi.org/10.1038/nature09968.

Gao, A.W., Canto, C., and Houtkooper, R.H. (2014). Mitochondrial response to nutrient availability and its role in metabolic disease. EMBO Mol. Med. *6*, 580–589. https://doi.org/10.1002/emmm.201303782.

Gao, Q., Binns, D.D., Kinch, L.N., Grishin, N.V., Ortiz, N., Chen, X., and Goodman, J.M. (2017). Pet10p is a yeast perilipin that stabilizes lipid droplets and promotes their assembly. J. Cell Biol. *216*, 3199–3217. https://doi.org/10.1083/jcb.201610013.

Goldstein, J.L., Basu, S.K., and Brown, M.S. (1983). Receptor-mediated endocytosis of low-density lipoprotein in cultured cells. Methods Enzymol. *98*, 241–260. https://doi.org/10.1016/0076-6879(83)98152-1.

Hayashi, T., Rizzuto, R., Hajnoczky, G., and Su, T.P. (2009). MAM: more than just a housekeeper. Trends Cell Biol. *19*, 81–88. https://doi.org/10.1016/j.tcb.2008.12.002.

Herzig, S., and Shaw, R.J. (2018). AMPK: guardian of metabolism and mitochondrial homeostasis. Nat. Rev. Mol. Cell Biol. *19*, 121–135. https://doi.org/10.1038/nrm.2017.95.

Holtta-Vuori, M., Salo, V.T., Ohsaki, Y., Suster, M.L., and Ikonen, E. (2013). Alleviation of seipinopathy-related ER stress by triglyceride storage. Hum. Mol. Genet. *22*, 1157–1166. https://doi.org/10.1093/hmg/dds523.

Joubert, M., Jagu, B., Montaigne, D., Marechal, X., Tesse, A., Ayer, A., Dollet, L., Le May, C., Toumaniantz, G., Manrique, A., et al. (2017). The sodium-glucose cotransporter 2 inhibitor dapagliflozin prevents cardiomyopathy in a diabetic lipodystrophic mouse model. Diabetes *66*, 1030–1040. https://doi.org/10.2337/db16-0733.

Kusminski, C.M., and Scherer, P.E. (2012). Mitochondrial dysfunction in white adipose tissue. Trends Endocrinol. Metab. *23*, 435–443. https://doi.org/10.1016/j.tem.2012.06.004.

Langfelder, P., and Horvath, S. (2007). Eigengene networks for studying the relationships between co-expression modules. BMC Syst. Biol. *1*, 54. https://doi.org/10.1186/1752-0509-1-54.

Liu, L., Jiang, Q., Wang, X., Zhang, Y., Lin, R.C., Lam, S.M., Shui, G., Zhou, L., Li, P., Wang, Y., et al. (2014). Adipose-specific knockout of SEIPIN/BSCL2 results in progressive lipodystrophy. Diabetes *63*, 2320–2331. https://doi.org/10.2337/db13-0729.

Love, M.I., Huber, W., and Anders, S. (2014). Moderated estimation of fold change and dispersion for RNA-seq data with DESeq2. Genome Biol. *15*, 550. https://doi.org/10.1186/s13059-014-0550-8.

Magre, J., Delepine, M., Khallouf, E., Gedde-Dahl, T., Jr., Van Maldergem, L., Sobel, E., Papp, J., Meier, M., Megarbane, A., Bachy, A., et al. (2001). Identification of the gene altered in Berardinelli-Seip congenital lipodystrophy on chromosome 11q13. Nat. Genet. *28*, 365–370. https://doi.org/10.1038/ng585.

Mayhew, T.M. (2011). Mapping the distributions and quantifying the labelling intensities of cell compartments by immunoelectron microscopy: progress towards a coherent set of methods. J. Anat. *219*, 647–660. https://doi.org/10.1111/j.1469-7580.2011.01438.x.

McIlroy, G.D., Suchacki, K., Roelofs, A.J., Yang, W., Fu, Y., Bai, B., Wallace, R.J., De Bari, C., Cawthorn, W.P., Han, W., et al. (2018). Adipose specific disruption of seipin causes early-onset generalised lipodystrophy and altered fuel utilisation without severe metabolic disease. Mol. Metab. *10*, 55–65. https://doi.org/10.1016/j.molmet.2018.01.019.

McLean, I.W., and Nakane, P.K. (1974). Periodate-lysine-paraformaldehyde fixative. A new fixation for immunoelectron microscopy. J. Histochem. Cytochem. *22*, 1077–1083. https://doi.org/10.1177/22.12.1077.

Mellacheruvu, D., Wright, Z., Couzens, A.L., Lambert, J.P., St-Denis, N.A., Li, T., Miteva, Y.V., Hauri, S., Sardiu, M.E., Low, T.Y., et al. (2013). The CRAPome: a contaminant repository for affinity purification-mass spectrometry data. Nat. Methods *10*, 730–736. https://doi.org/10.1038/nmeth.2557.

Millard, P., Delepine, B., Guionnet, M., Heuillet, M., Bellvert, F., and Letisse, F. (2019). IsoCor: isotope correction for high-resolution MS labeling experiments. Bioinformatics *35*, 4484–4487. https://doi.org/10.1093/bioinformatics/btz209.

Nguyen, T.B., Louie, S.M., Daniele, J.R., Tran, Q., Dillin, A., Zoncu, R., Nomura, D.K., and Olzmann, J.A. (2017). DGAT1-dependent lipid droplet biogenesis protects mitochondrial function during starvation-induced autophagy. Dev. Cell *42*, 9–21.e5. https://doi.org/10.1016/j.devcel.2017.06.003.

Pagac, M., Cooper, D.E., Qi, Y., Lukmantara, I.E., Mak, H.Y., Wu, Z., Tian, Y., Liu, Z., Lei, M., Du, X., et al. (2016). SEIPIN regulates lipid droplet expansion and adipocyte development by modulating the activity of glycerol-3-phosphate acyltransferase. Cell Rep. *17*, 1546–1559. https://doi.org/10.1016/j.celrep.2016.10.037.

Payne, V.A., Grimsey, N., Tuthill, A., Virtue, S., Gray, S.L., Dalla Nora, E., Semple, R.K., O'Rahilly, S., and Rochford, J.J. (2008). The human lipodystrophy gene BSCL2/seipin may be essential for normal adipocyte differentiation. Diabetes *57*, 2055–2060. https://doi.org/10.2337/db08-0184.

Perez-Riverol, Y., Csordas, A., Bai, J., Bernal-Llinares, M., Hewapathirana, S., Kundu, D.J., Inuganti, A., Griss, J., Mayer, G., Eisenacher, M., et al. (2019). The PRIDE database and related tools and resources in 2019: improving support for quantification data. Nucleic Acids Res. *47*, D442–D450. https://doi.org/10.1093/nar/gky1106.

Perkins, D.N., Pappin, D.J., Creasy, D.M., and Cottrell, J.S. (1999). Probability-based protein identification by searching sequence databases using mass spectrometry data. Electrophoresis *20*, 3551–3567. https://doi.org/10.1002/(SICI)1522-2683(19991201)20:18<3551::AID-ELPS3551>3.0.CO;2.

Poullet, P., Carpentier, S., and Barillot, E. (2007). myProMS, a web server for management and validation of mass spectrometry-based proteomic data. Proteomics *7*, 2553–2556. https://doi.org/10.1002/pmic.200600784.

Prasanna, X., Salo, V.T., Li, S., Ven, K., Vihinen, H., Jokitalo, E., Vattulainen, I., and Ikonen, E. (2021). Seipin traps triacylglycerols to facilitate their nanoscale clustering in the endoplasmic reticulum membrane. PLoS Biol. *19*, e3000998. https://doi.org/10.1371/journal.pbio.3000998.

Prieur, X., Dollet, L., Takahashi, M., Nemani, M., Pillot, B., Le May, C., Mounier, C., Takigawa-Imamura, H., Zelenika, D., Matsuda, F., et al. (2013). Thiazolidinediones partially reverse the metabolic disturbances observed in Bscl2/seipin-deficient mice. Diabetologia *56*, 1813–1825. https://doi.org/10.1007/s00125-013-2926-9.

Pulli, I., Lassila, T., Pan, G., Yan, D., Olkkonen, V.M., and Tornquist, K. (2018). Oxysterol-binding protein related-proteins (ORPs) 5 and 8 regulate calcium signaling at specific cell compartments. Cell Calcium *72*, 62–69. https://doi.org/10.1016/j.ceca.2018.03.001.

Pulli, I., Lof, C., Blom, T., Asghar, M.Y., Lassila, T., Back, N., Lin, K.L., Nystrom, J.H., Kemppainen, K., Toivola, D.M., et al. (2019). Sphingosine kinase 1 overexpression induces MFN2 fragmentation and alters mitochondrial matrix Ca(2+) handling in HeLa cells. Biochim. Biophys. Acta Mol. Cell Res. *1866*, 1475–1486. https://doi.org/10.1016/j.bbamcr.2019.06.006.

Salo, V.T., Belevich, I., Li, S., Karhinen, L., Vihinen, H., Vigouroux, C., Magre, J., Thiele, C., Holtta-Vuori, M., Jokitalo, E., and Ikonen, E. (2016). Seipin regulates ER-lipid droplet contacts and cargo delivery. EMBO J. *35*, 2699–2716. https://doi.org/10.15252/embj.201695170.

Salo, V.T., Hölttä-Vuori, M., and Ikonen, E. (2020). Seipin-mediated contacts as gatekeepers of lipid flux at the endoplasmic reticulum–lipid droplet nexus. Contact *3*, 2515256420945820. https://doi.org/10.1177/2515256420945820.

Salo, V.T., Li, S., Vihinen, H., Holtta-Vuori, M., Szkalisity, A., Horvath, P., Belevich, I., Peranen, J., Thiele, C., Somerharju, P., et al. (2019). Seipin facilitates triglyceride flow to lipid droplet and counteracts droplet ripening via endoplasmic reticulum contact. Dev. Cell *50*, 478–493 e479. https://doi.org/10.1016/j.devcel.2019.05.016.

Sassmann, A., Offermanns, S., and Wettschureck, N. (2010). Tamoxifen-inducible Cre-mediated recombination in adipocytes. Genesis *48*, 618–625. https://doi.org/10.1002/dvg.20665.

Sim, M.F., Dennis, R.J., Aubry, E.M., Ramanathan, N., Sembongi, H., Saudek, V., Ito, D., O'Rahilly, S., Siniossoglou, S., and Rochford, J.J. (2012). The human lipodystrophy protein seipin is an ER membrane adaptor for the adipogenic PA phosphatase lipin 1. Mol. Metab. *2*, 38–46. https://doi.org/10.1016/j.molmet.2012.11.002.

Solenski, N.J., diPierro, C.G., Trimmer, P.A., Kwan, A.L., and Helm, G.A. (2002). Ultrastructural changes of neuronal mitochondria after transient and permanent cerebral ischemia. Stroke *33*, 816–824. https://doi.org/10.1161/hs0302.104541.

Spandl, J., White, D.J., Peychl, J., and Thiele, C. (2009). Live cell multicolor imaging of lipid droplets with a new dye, LD540. Traffic *10*, 1579–1584. https://doi.org/10.1111/j.1600-0854.2009.00980.x.

Suzuki, J., Kanemaru, K., Ishii, K., Ohkura, M., Okubo, Y., and Iino, M. (2014). Imaging intraorganellar Ca^{2+} at subcellular resolution using CEPIA. Nat. Commun. *5*, 4153. https://doi.org/10.1038/ncomms5153.

Szymanski, K.M., Binns, D., Bartz, R., Grishin, N.V., Li, W.P., Agarwal, A.K., Garg, A., Anderson, R.G., and Goodman, J.M. (2007). The lipodystrophy protein seipin is found at endoplasmic reticulum lipid droplet junctions and is important for droplet morphology. Proc. Natl. Acad. Sci. U S A *104*, 20890–20895. https://doi.org/10.1073/pnas.0704154104.

Talukder, M.M., Sim, M.F., O'Rahilly, S., Edwardson, J.M., and Rochford, J.J. (2015). Seipin oligomers can interact directly with AGPAT2 and lipin 1, physically scaffolding critical regulators of adipogenesis. Mol. Metab. *4*, 199–209. https://doi.org/10.1016/j.molmet.2014.12.013.

Theurey, P., and Rieusset, J. (2017). Mitochondria-associated membranes response to nutrient availability and role in metabolic diseases. Trends Endocrinol. Metab. *28*, 32–45. https://doi.org/10.1016/j.tem.2016.09.002.

Theurey, P., Tubbs, E., Vial, G., Jacquemetton, J., Bendridi, N., Chauvin, M.A., Alam, M.R., Le Romancer, M., Vidal, H., and Rieusset, J. (2016). Mitochondria-associated endoplasmic reticulum membranes allow adaptation of mitochondrial metabolism to glucose availability in the liver. J. Mol. Cell Biol. *8*, 129–143. https://doi.org/10.1093/jmcb/mjw004.

Tubbs, E., and Rieusset, J. (2016). Study of endoplasmic reticulum and mitochondria interactions by in situ proximity ligation assay in fixed cells. J. Vis. Exp. https://doi.org/10.3791/54899.

Wang, H., Becuwe, M., Housden, B.E., Chitraju, C., Porras, A.J., Graham, M.M., Liu, X.N., Thiam, A.R., Savage, D.B., Agarwal, A.K., et al. (2016). Seipin is required for converting nascent to mature lipid droplets. eLife *5*. https://doi.org/10.7554/eLife.16582.

Wescott, A.P., Kao, J.P.Y., Lederer, W.J., and Boyman, L. (2019). Voltage-energized calcium-sensitive ATP production by mitochondria. Nat. Metab. *1*, 975–984. https://doi.org/10.1038/s42255-019-0126-8.

Wieckowski, M.R., Giorgi, C., Lebiedzinska, M., Duszynski, J., and Pinton, P. (2009). Isolation of mitochondria-associated membranes and mitochondria from animal tissues and cells. Nat. Protoc. *4*, 1582–1590. https://doi.org/10.1038/nprot.2009.151.

Williams, G.S., Boyman, L., and Lederer, W.J. (2015). Mitochondrial calcium and the regulation of metabolism in the heart. J. Mol. Cell Cardiol. *78*, 35–45. https://doi.org/10.1016/j.yjmcc.2014.10.019.

Wisniewski, J.R., Zougman, A., Nagaraj, N., and Mann, M. (2009). Universal sample preparation method for proteome analysis. Nat. Methods *6*, 359–362. https://doi.org/10.1038/nmeth.1322.

Wu, X., Liu, X., Wang, H., Zhou, Z., Yang, C., Li, Z., Zhang, Y., Shi, X., Zhang, L., Wang, Y., et al. (2021). Seipin deficiency accelerates heart failure due to calcium handling abnormalities and endoplasmic reticulum stress in mice. Front. Cardiovasc. Med. *8*, 644128. https://doi.org/10.3389/fcvm.2021.644128.

Xiong, J., Sun, P., Wang, Y., Hua, X., Song, W., Wang, Y., Wu, J., Yu, W., Liu, G., and Chen, L. (2020). Heterozygous deletion of Seipin in islet beta cells of male mice has an impact on insulin synthesis and secretion through reduced PPARgamma expression. Diabetologia *63*, 338–350. https://doi.org/10.1007/s00125-019-05038-x.

Zhang, B., and Horvath, S. (2005). A general framework for weighted gene co-expression network analysis. Stat. Appl. Genet. Mol. Biol. *4*, 17. https://doi.org/10.2202/1544-6115.1128.

Zhou, H., Lei, X., Benson, T., Mintz, J., Xu, X., Harris, R.B., Weintraub, N.L., Wang, X., and Chen, W. (2015). Berardinelli-Seip congenital lipodystrophy 2 regulates adipocyte lipolysis, browning, and energy balance in adult animals. J. Lipid Res. *56*, 1912–1925. https://doi.org/10.1194/jlr.M060244.

STAR★METHODS

KEY RESOURCES TABLE

REAGENT or RESOURCE	SOURCE	IDENTIFIER
Antibodies		
anti-HA antibody (mouse)	Biolegend	901502 RRID:AB_2565007
anti-HA antibody (rabbit)	Cell signalling	3724 RRID:AB_1549585
anti-Calreticulin antibody (mouse)	Abcam	ab22683 RRID:AB_447253
anti-SERCA2 antibody (mouse)	Santa Cruz	sc376235 RRID:AB_10989947
anti Phospho-AMPk (Thr172) antibody (rabbit)	Cell signalling	2535 RRID:AB_331250
anti-AMPK antibody (rabbit)	Cell signalling	5831 RRID:AB_10622186
anti-GRP75 antibody (rabbit)	Cell signalling	3593 RRID:AB_2120328
anti-VDAC antibody (rabbit)	Abcam	ab15895 RRID:AB_2214787
anti-ATPIF1 antibody (mouse)	Thermofisher	A-21355 RRID:AB_2535841
anti-SERCA2 antibody (mouse)	Abcam	ab2861 RRID:AB_2061425
anti-IP3R-1-2-3 antibody (mouse)	Santa cruz	sc377518 RRID:AB_2637028
anti-IP3R-3 antibody (rabbit)	Abcam	ab5804 RRID:AB_305124
anti-perilipin1 antibody (mouse)	Progen	651156 RRID:AB_1542731
Anti-tubulin antibody (mouse)	Sigma	T9026 RRID:AB_477593
anti-beta actin antibody (mouse)	Sigma	A5316 RRID:AB_476743
anti-HA magnetic beads	Thermofisher	88837 RRID:AB_2533052
anti-GFP antibody (rabbit)	Abcam	ab290 RRID:AB_303395
anti-GFP antibody (mouse)	Abcam	ab1218 RRID:AB_298911
anti-SERCA2 antibody (mouse)	Novus Biological	NB300-529 RRID:AB_2061435
anti-IP3R-3 antibody (mouse)	BD Transduction Lab	610312 RRID:AB_397704
1.4 nm nanogold-conjugated anti-rabbit secondary antibody	Nanoprobes	2004, RRID:AB_2631182
Bacterial and virus strains		
Edit-R Inducible Lentiviral hEF1a-Blast-Cas9 Nuclease Particles	Horizon	VCAS11227
Chemicals, peptides, and recombinant proteins		
Rhod-2 AM	Thermofisher	R1244
Fluo-4, AM	Thermofisher	F14201
Fura-2 AM	Life Technologies	F088
Oleic acid	Sigma-Aldrich	0-1383
Dapi	Sigma-Aldrich	D9542
LD540	Princeton BioMolecular Research	Spandl et al.(2009)
LipidtoxDeep Red	Thermo Fisher	H34477
Mitotracker Deep Red	Thermo Fisher	M22426
Geneticin, G418 (0.6 mg/ml)	Thermo Fisher	11811-031-Gibco
Puromycin (1μg/ml)	Sigma-Aldrich	P8833
LPDS (lipoprotein deficient serum)	Prepared as described in Goldstein, J.L, 1983	N/A
Indole-3-acetic acid sodium, IAA (500 μM)	Santa Cruz	sc-215171
Cell-SIR647 (0.3 μM)	New England BioLabs	S9102S
Prolong Live Anti-Fade	Thermo Fisher	P36975
Sodium citrate	Riedel-de-Haën	32320
caged(1,4,5)IP3/PM	Sichem	cag-iso-2-145-100

(*Continued on next page*)

Continued

REAGENT or RESOURCE	SOURCE	IDENTIFIER
Critical commercial assays		
Duolink™ In Situ Red	Sigma-Aldrich	#DUO92101
Duolink™ In Situ FarRed	Sigma-Aldrich	#DUO92013
Nextera DNA Sample Prep kit	Illumina	FC-121-1030
Amaxa cell line nucleofector kit	LONZA	VCA-10003
ATP determination kit	Thermofisher	A22066
HIDEX Sense plate reader	Hidex Corporation	N/A
Lipofectamine LTX with PLUS	Thermo Fisher	A12621
Turbofect	Thermo Fisher	R0531
Deposited data		
Mass spectrometry proteomic	ProteomeXchange Consortium	http://www.ebi.ac.uk/pride
		Permanent identifier: PXD02967
3'seq-RNA profiling data of iATSKO and control mice	GEO	https://www.ncbi.nlm.nih.gov/geo/
		Permanent identifier: GSE188544
Experimental models: Cell lines		
3T3-L1	ATCC	CL-173
A431	ATCC	CRL-1555
BSCL patient lymphoblasts	Vigouroux's lab	Boutet et al. (2009)
Experimental models: Organisms/strains		
C57BL6J *Bscl2*$^{lox/lox}$	European Mouse Mutant Cell Repository	N/A
C57BL6J ERT2-Adipoq-CRE	Pr S Offermanns lab (Max Plank institute)	Sassmann et al. (2010)
Oligonucleotides		
On-target-plus siRNA smart pool againt mouse Bscl2	Horizon	L-040550-01-0005
On-target-plus siRNA non targetting pool	Horizon	D-001810-10
crRNA for CRISPR/CAS9 editing	Integrated DNA technologies	Gaggaattcacccttgttc
modified single-strand oligonucleotide donor for CRISPR/CAS9 editing	Integrated DNA technologies	CAAGGGAAAAGGTGTATGATGGGAAAGC GCTGGAATGTGAGTAATTCACACTTTGTT CAAGCGTAATCTGGAACATCGTATGGGT AAGCGTAATCTGGAACATCGTATGGGTA AGCGTAATCTGGAACATCGTATGGGTAG GAACTGGAGCAGGTCGGGCGTTGCCTG AGGCTACCCAGAGTCTCAGGGGCAAGG GCAGA
Oligonucleotides for Real-time quantitative PCR	Eurofins	Table S3
Recombinant DNA		
pGL3-sgIP3R3.N-Cas9-T2A-mCherry-P2A-Puro	This study	N/A
pCMV-CEPIA2mt	Addgene	Suzuki et al. (2014), Addgene 58218
Mitochondrially targeted aequorin	Pinton lab	Bonora et al. (2013)
Cytosolic aequorin	Pinton lab	Bonora et al. (2013)
pGL3-basic-IP3R3-sfGFP(N) HDR template	This study	N/A
BFP-Mito	Addgene	Friedman et al. (2011), Addgene 49151
Software and algorithms		
MetaMorph	Molecular devices	
MassLynx	Waters	
TargetLynx	Waters	
IsoCor: isotope correction for high-resolution MS labeling experiments		https://doi.org/10.1093/bioinformatics/btz209
Deseq2	R package	Love et al. (2014)

(*Continued on next page*)

Continued

REAGENT or RESOURCE	SOURCE	IDENTIFIER
MaSigPro		Conesa et al. (2006)
Weighted correlation network analysis		Langfelder and Horvath (2007)
MyPROMS		Poullet et al. (2007)
ImageJ Fiji		https://fiji.sc/
CellProfiler		https://cellprofiler.org/
		Carpenter et al. (2006)
Matlab	Mathworks	www.mathworks.com/products/matlab.html
Ilastik		www.ilastik.org
		Berg et al. (2019)
Huygens Professional	Scientific Volume Imaging	https://svi.nl/Huygens-Professional
CorelDraw	Corel Corporation	https://www.corel.com/en
Microscopy Image Browser		http//mib.helsinki.fi
		Belevich et al. (2016)
Mascott	Matrix science	version 2.2.51
		Perkins et al. (1999)

RESOURCE AVAILABILITY

Lead contact

Further information and requests for resources and reagents should be directed to and will be fulfilled by the lead contact, Xavier Prieur (xavier.prieur@univ-nantes.fr)

Materials availability

- The iATSKO Mouse line generated in this study is available from the lead contact with a completed Materials Transfer Agreement.
- Tagged A431 IP3R cells and S-HA 3T3-L1 cells generated in this study are available from the lead contact with a completed Materials Transfer Agreement.
- The plasmids generated in this study (pGL3-basic-IP3R3-sfGFP(N) HDR template and pGL3-sgIP3R3.N-Cas9-T2A-mCherry-P2A-Puro) are available from the Lead Contact with a completed Materials Transfer Agreement

Data and code availability

- 3'seq-RNA profiling data of iATSKO and control mice adipose tissue have been deposited at GEO and are publicly available as of the date of publication. The dataset identifier is GSE188544 and is listed in the key resources table.
- Mass spectrometry proteomic analysis of the seipin-HA immunoprecipitation products data have been deposited to the ProteomeXchange Consortium via the PRIDE (Perez-Riverol et al., 2019) and are publicly available as of the date of publication with the dataset identifier PXD02967, listed in the key resources table.
- All microscopy data, metabolites quantification, QPCR analysis and western-blot quantification, will be share by the lead contact upon request.
- This paper does not report original code.
- Any additional information required to reanalyze the data reported in this paper is available from the lead contact upon request.

EXPERIMENTAL MODEL AND SUBJECT DETAILS

Cell culture: A431 cells, lymphoblasts, and 3T3-L1 adipocytes

A431 cells (ATCC CRL-1555, sex: female) were maintained in Dulbecco's modified Eagle's medium (DMEM) containing 10% fetal bovine serum (FBS), penicillin/streptomycin (100 U/ml each), L-glutamine (2mM) at 37°C in 5% CO_2. Transfections of plasmids into A431 cells was done using Lipofectamine LTX with PLUS Reagent or Turbofect according to the manufacturer's instructions. Cells were delipidated by culturing in serum-free medium supplemented with 5% lipoprotein deficient serum (LPDS, prepared as described in(Goldstein et al., 1983)) for indicated times. For LD induction cells were supplemented with 0.2 mMOA (final concentration, OA in complex with BSA in 8:1 molar ratio prepared in serum-free DMEM as described previously (Holtta-Vuori et al.,

2013)) for indicated times. For depletion of seipin, IAA was added to the medium for indicated times, vehicle control was Milli-Q-H_2O (1:100).

Epstein Barr-virus transformed lymphoblasts derived from BSCL2 patients S1 (compound heterozygous missense A212P mutation and truncation mutation), S3, S5 and S9 (homozygous truncation mutations) have been described (Boutet et al., 2009) and were maintained in RPMI 1640 medium supplemented with 15% FBS, penicillin/streptomycin (100 U/mL each), L-glutamine (2mM) at 37°C in 5% CO_2.

3T3-L1 cells were maintained in medium A (DMEM glucose 4.5g/L, 10% calf serum, 1% Penicilin/streptomycin, 1% glutamine). Cells were seeded at a density of 20,000 cells/mL in medium B (DMEM glucose 4.5g/L, 10% FCS, 1% Penicilin/streptomycin, 1% glutamine) and adipocyte differentiation was induced 2 days after confluence in medium B with 2μM insulin, 500 mM IBMX and 1μM dexamethasone (differentiation media induction, DMI). On day 3, medium was changed to medium B supplemented with 2mM insulin and from day 6, wells were switched back to medium B. For siRNA experiments, at day 6 of differentiation in T75 flask, cells are dissociated with TrypleE express (Thermofisher) and resuspended in medium B (12 mL/Flask). The siRNA mix (20nM siRNA, 2.5 μL Lipofectamine RNAi max, Thermofisher, 47.5μL of OptiMEM, Thermofisher), is added to a collagen IV precoated well of ibidi 8 well plate, and 0.25 mL of differentiated adipocyte suspension is added for reverse transfection. 72 hours after, the assays (calcium or PLA) are performed. siBSCL2 pool are obtained from Horizon.

Stable A431 cell lines

End-seipin-sfGFP cells have been described (Salo et al., 2016). End-seipin-GFPx7 cells stably expressing BFP-KDEL have been described (Salo et al., 2019). For generation of a stable clone expressing a mitochondrial marker, these cells were transfected with mito-BFP (Addgene #49151), a gift from Gia Voeltz (Friedman et al., 2011), selected in G418 and a single clone was isolated by limiting dilution. Seipin KO cells stably expressing WT- or A212P-seipin-GFP have been described (Salo et al., 2016). Seipin degron-A and seipin degron-B cells and seipin degron control cells have been described (Salo et al., 2019). For the data in Figures 3G and 3H and Figures S2A and S2B seipin degron B and another clone generated with the same strategy was utilized. For the data in Figures 3I and 3J, seipin degron control, degron-A and seipin degron-B cells were transfected with pCMV-CEPIA2mt (Addgene #58218, a gift from Masamitsu Iino (Suzuki et al., 2014)) and a semistable pool was selected using G418 and FACS-sorted FACS with BD Influx Flow Cytometer (BD Biosciences, USA) at HiLIFE Biomedicum Flow cytometry unit, University of Helsinki, for similar fluorescence level.

Construction of end-sfGFP-IP3R cells

Endogenous tagging of IP3R was performed as described (Salo et al., 2019). Briefly, sfGFP (Addgene #56482 a gift from Michael Davidson) was amplified by PCR and integrated into the homology directed repair (HDR) template to insert into the genomic locus of IP3R type 3 (NM_002224.4) N-terminus. Recombination templates and sgRNAs are described in Figure S1E. The HDR template and Cas9 was transfected into end-seipin-sSNAPf cells (Salo et al., 2019) and cells were FACS sorted with BD Influx Flow Cytometer (BD Biosciences, USA) at HiLIFE Bio- medicum Flow cytometry unit, University of Helsinki, for GFP fluorescence after transient selection with puromycin. Single clones were isolated by limiting dilution and homozygous knock-in validated by genomic PCR. Seipin knockout was performed on top of these cells using CRISPR/Cas9 as described (Salo et al., 2016) and a single clone was isolated using limiting dilution and verified by the seipin KO LD phenotype.

Generation of end-seipin-HA cells in 3T3L1-cells

3T3-L1 Cas9 inducible population was first generated. 3T3-L1 cells in 6-well plates were transduced with Edit-R inducible Lentiviral Cas 9 (MOI 10) encoding blasticidin resistance gene (Dharmacon, Inc.). The next day, cells were selected with 10 $\mu g.mL^{-1}$ blasticidin and passaged in T75 flask. Selection was maintained for 6 days before further culturing or freezing. The resulting cells were considered the 3T3-L1 Cas9 inducible cell mixed population. Using CRISPR/Cas9 technology, endogenous seipin was tagged with 3 hemagglutinin tags (HAX3). Cas9 expression was induced with Doxycycline 1 $\mu g.mL^{-1}$ final 72 h before a chemically modified single-strand oligonucleotide donor was electroporated with pre-assembled crRNA + tracrRNA complexes in 3T3-L1-Cas9 population to insert 3 copies of HA tag into the genomic locus of seipin C-terminus. (Alt-R CRISPR-Cas9 System and PAGE ultramer DNA oligo phosphorothioate bond, Integrated DNA Technologies; Amaxa cell line nucleofector kit V VCA-10003, LONZA). Single clones were isolated by limiting dilution in 96-well plates. These clones were further tested for heterozygous tagging using genomic PCR. The heterozygous end-seipin HA cell line was validated by western blot and fluorescence microscopy for HA signal and proper subcellular localization with antibody against HA (mouse mAb anti-HA Biolegend#901501 or rabbit mAb anti-HA cell signaling#3724) and by Oil Red O-staining for adipogenic differentiation. We call these cells S-HA 3T3-L1.

Animals

Bscl2$^{lox/lox}$ was established at the Institut Clinique de la Souris (http://www.phenomin.fr). Three clones were ordered from the European Mouse Mutant Cell Repository (https://www.eummcr.org/). All three clones were validated by Southern blot (internal Neo probe) and PCR confirmation of the presence of the 3' LoxP site. Clone HEPD0757_2_A10 was karyotyped by chromosome spreading and Giemsa staining and microinjected in BALB/cN blastocysts. Resulting male chimeras were obtained and germ line transmission was achieved for the tm1a allele (knock-out first with conditional potential). The KO allele (tm1b) was obtained after breeding tm1a animals

with a Cre deleter line (Birling et al., 2012) and phenotyped by PHENOMIN-ICS. All data are freely available through the IMPC web site (https://www.mousephenotype.org/data/genes/MGI:1298392). The cKO Bscl2 allele (tm1c; Lox/Lox) was obtained by breeding the tm1a allele with a Flp deleter line (Birling et al., 2012). *Bscl2*$^{lox/lox}$ mice were crossed with ERT2-Adipoq-CRE (Sassmann et al., 2010) mice to generate Bscl2$^{lox/lox}$ mice X ERT2-Adipoq-CRE mice. Mice were housed at 21°C with a 12:12 h light-dark cycle with free access to food and water. CRE activation was performed by 5 days intraperitoneal injection of tamoxifen resuspend in sunflower oil: ethanol (9:1) to 8 weeks-old males. For the 3-month group, one intraperitoneal injection was repeated every month. Glucose tolerance test and Insulin tolerance test were performed after 6-hours fasting as previously described (Prieur et al., 2013). All mice (males, n = 8 to 11 per group) were euthanized in the random fed state between 8 a.m to 10 a.m. The ethics committee of the French national veterinary agency approved all animal protocols used in this study.

Food was removed 6 h before the initiation of the intra-peritoneal glucose tolerance test (IPGTT) or the insulin tolerance test (ITT). At time 0, a single dose of glucose (2 g/kg) or insulin (0.75 U/kg, actrapid, Novo Nordisk) was injected *i.p.* and blood glucose levels were monitored using a glucometer (Freestyle Papillon, Abbott, France) on 2.5 μl samples collected from the tail.

METHODS DETAILS

Subcellular fractionation and immunoblotting

The subcellular fractionation from mouse inguinal adipose tissue or 3T3-L1 adipocytes was performed based on published protocols(Arruda et al., 2014; Fu et al., 2011; Wieckowski et al., 2009) with minor modifications. Twenty 6-well plates for 3T3L-1 or 1.2 g of WAT are enough to isolate crude mitochondrial fraction needed to purify the mitochondrial-associated membrane (MAM) fraction and pure mitochondrial fraction.

For Figure 2I, S-HA 3T3-L1 cells were washed twice with PBS (without Ca^{2+} and Mg^{2+}) and trypsin was added to detach cells. Cells were harvested and centrifuged at 600 g for 5 min at 4°C. The supernatant was discarded and cells re-suspended in PBS (with Ca^{2+} and Mg^{2+}) before a second centrifugation at 600g for 5 min at 4°C. The pellet was precooled in STM buffer (250 mM sucrose, 50 mM Tris, HCl (pH 7.4), 5 mM $MgCl_2$) in an ice-bath before starting the homogenization step using a Teflon pestle. The homogenate was transferred to a 15-ml polypropylene centrifugation tube and centrifuged twice at 600 g for 5 min at 4°C. The supernatant was recovered and further centrifuged for 15 min at 10500 g, using an ultra-Optima Max.XP Beckman Coulter instrument, in a MLA.130 rotor. The resulting pellet (crude mitochondrial fraction) was collected and the supernatant was stored at 4°C to proceed with further separation of cytosolic, lysosomal and ER fractions.

For Figures 7G and 7H, fresh WAT (1.2g) was immediately weighed and transferred in PBS. The tissue was minced and submitted to collagenase type I digestion (25 g/kg) in DMEM medium supplemented with 10% SVF, 60 min at 37°C under stirring (90 rpm). The enzyme was neutralized and the solution centrifuged for 10 min at 700 g. Digestion released floating adipocytes. The adipocyte ring was resuspended in cold STM buffer and the cells were disrupted successively with 18- and 23-gauge needles. The homogenate was centrifuged at 700 g for 10 min; the supernatant was recovered and further centrifuged for 15 min at 10500 g. The resulting pellet (crude mitochondrial fraction) was collected and the supernatant was saved for gathering the ER fraction.

The crude mitochondrial fraction was directly analyzed or was layered in a 30 % Percoll gradient in mitochondria re-suspending buffer (MRB: Manitol 225 mM, Hepes 5 mM (pH 7.4), EGTA 0.5 mM) and centrifuged at 95000 g for 30 min using a Beckman Ultra centrifuge Optima L-80XP-432 in a 41 SW rotor. The obtained pure mitochondrial fraction was recovered at the bottom of the tube while MAMs were identified as an intermediate layer between the light membrane and the pure mitochondrial fractions. The pure mitochondrial fraction was collected, diluted in MRB buffer and further centrifuged at 6300 g. The pellet was re-suspended in MRB buffer. The MAM fraction was collected and diluted in MRB buffer. The suspension was centrifuged at 100.000 g for 1 h. The pellet was re-suspended in small volume of MRB buffer. The ER fraction was obtained by centrifuging the supernatant collected from the 10500 g centrifugation step at 100.000 g for 1 h. This results in the isolation of ER (pellet) and cytosolic fraction (supernatant). Protein concentration was determined by BCA and 25 μg of protein were separated by SDS-PAGE and immunoblotted as indicated in the figure legends.

For immunoblotting cells were lysed in buffer containing 1.0% Igepal CA-630, 0.05%-0.5% sodium deoxycholate, 0.1% sodium dodecyl sulfate, 250 mM Tris-HCl, pH. 7.5 and 150 mM NaCl with protease inhibitors. Lysate was cleared by centrifugation at 13 000 g for 10 min at +4°c. Equal amounts of protein were loaded onto polyacrylamide gels. Membranes were blocked with 5% milk in TBS containing 0.1% Tween-20 for 1 h at RT, and subsequently probed with primary antibodies at 4°c overnight. After washing with TBS containing 0.1% Tween-20, membranes were incubated with secondary antibodies for 1 h at RT. Membranes were washed, incubated with ECL substrate, and imaged with a ChemiDoc Imaging System (Bio-Rad). Band intensities were quantified in ImageJ FIJI and normalized to total protein content quantified with the Stain-Free technology (Bio-Rad).

PLA, immunofluorescence and LD analysis in A431 cells

PLA in A431 cells (Figure 3) was performed using Duolink™ In Situ Red Starter Kit Mouse/Rabbit (#DUO92101, Merck) according to manufacturer's instructions. Briefly, cells were first washed with PBS, fixed with either 4% PFA in 250mMHepes, pH 7.4, 100 mM $CaCl_2$ and 100 mM$MgCl_2$ for 20 min at RT (for PLA with seipin-GFP together with SERCA or IP3R) or with methanol for 2 min on ice (for PLA with seipin-GFP together with VDAC1). Fixing was followed by quenching in 50 mM NH_4Cl for 10 min and 3 washes with PBS. Cells were then permeabilized using 0.01% Triton-X in PBS. Blocking was performed for 60 min at 37°C using Duolink

Blocking Solution. Antibody incubations were performed using the following dilutions in Duolink Antibody Diluent: rabbit anti-GFP 1:1000 (Abcam ab290), mouse anti-SERCA2 1:200 (Novus NB300-529), mouse anti-IP3R 1:500 (BD Transduction Lab 610312), mouse anti-GFP (ab1218, 1:250) and rabbit anti-VDAC1 (ab1589, 1:100). Antibody incubations were performed for 90 min at RT (for PLA with seipin-GFP together with SERCA or IP3R) or 60 min at +37 (for PLA with seipin-GFP and VDAC1). Subsequent reactions were performed exactly as recommended in the kit instructions and cell nuclei were finally stained with DAPI 10 μg/ml (Sigma-Aldrich, # D9542). Z-stacks of cells were acquired with Nikon Eclipse Ti-E microscope equipped with 40x air objective, NA0.75, and deconvolved using Huygens Professional and maximum intensity projections were generated in Matlab. Cell boundaries and PLA foci were segmented and the number of PLA foci/cell was analyzed using CellProfiler (Carpenter et al., 2006) coupled with custom Matlab software generated for post-processing reported previously (Salo et al., 2019). For the data in Figure 3C, PLA foci and mitochondria were imaged using Zeiss LSM 880×microscope equipped with Airyscan (Fast) detector, 63× microscope equipped with Airyscan (Fast) detector, 63x Plan-Apochromat oil objective, NA 1.4 and images Airyscan processed using Zeiss Zen software package with identical (default) settings for all acquisitions. Mitochondria were segmented using Ilastik (Berg et al., 2019) utilizing pixel + object classification mode and subsequent analysis of the fraction of PLA foci overlapping with mitochondria was performed in CellProfiler coupled with custom Matlab software generated for post-processing as above. For the data in Figure S1F, cells were stained with anti-IP3R antibodies as described above, except that blocking was done using 10% FBS in PBS. For the data in Figure S7A, LD analysis was done as described in (Salo et al., 2019). Cells were treated with IAA, citrate (from 1 M stock concentration in MqH20) and OA as indicated. After this, cells were fixed with PFA and quenched as described above. Then nuclei were stained with Dapi as described above and LDs were stained with LD540 (Spandl et al., 2009) (1: 10 000) for 20 min RT. Z-stacks of cells were acquired with Nikon Eclipse Ti-E microscope equipped with 60x oil objective, NA 1.4, with 1.5 zoom lens, and deconvolved using Huygens Professional and maximum intensity projections were generated in Matlab. Total LD areas/cell and LD size distributions were analyzed as described (Salo et al., 2019).

PLA in 3T3-L1 cells

PLA in 3T3-L1 cells (Figure 5) was performed using Duolink™ In Situ FarRed (#DUO92013, Sigma-Aldrich) according to manufacturer's instructions. Briefly, cells were first washed with PBS, fixed with 4% PFA for 10 min, followed by 3 washes with PBS. Cells were then permeabilized using 0.2% saponin in PBS. Blocking was performed for 60 min at RT using a solution 3%BSA, 0.1% saponin, 20 mM glycine in PBS. Primary antibodies incubations were performed for O/N at 4°C in 2%BSA, 0.1% saponin, 20 mM glycine in PBS with the following antibodies used as indicated: rabbit anti-HA 1:500 (Cell Signaling 3724), mouse anti-SERCA2 1:100 (Abcam 2861), mouse anti-IP3R1-2-3 1:100 (Santa Cruz 377518), rabbit anti-IP3R 1 :400 (Abcam 5804), mouse anti-Perilipin1 1:500 (Progen 651156), rabbit anti-VDAC1 1 :200 (Abcam 15895). Subsequent reactions were performed exactly as recommended in the kit instructions and cell nuclei were finally stained with DAPI before washing with a final solution of 200mM Tris-HCl, 137mM NaCl, 0.05% Tween20. Z-stacks of cells were acquired with Nikon A1RSi confocal system with 60x oil immersion objective. The number of PLA foci/cell was analyzed using ImageJ 2.0. Following parameters used throughout: nucleus size, 25-100 micron^2; dots size, 0-1 micron^2. Statistical analysis of the PLA results was performed using the Mann-Whitney test (Prism 7.0).

Live and fixed cell Airyscan microscopy and analysis

For all Airyscan microscopy, cells were plated onto 8-well Lab-Tek II #1.5 coverglass coated with 10 mg/ml fibronectin. For imaging of fixed samples, cells were kept in PBS after fixation and where indicated, LDs were stained using LipidTOX Deep Red (1:2000 for 20 min followed by washes with PBS). For live cell imaging, cells were imaged in +37C, 5% CO2 in Flurobrite DMEM medium supplemented with 10% FBS, penicillin/streptomycin (100 U/ml each), L-glutamine (2 mM) and Prolong Live Anti-Fade (1:100, Thermo Fisher P36975). Snap-labelling was performed as described[19]. Where indicated, mitochondria were stained using MitoTracker Deep Red (1:10 000 added to the imaging medium just prior to starting image acquisition). Imaging was performed using Zeiss LSM 880 confocal microscope equipped with Airyscan (Fast) detector, 63x Plan-Apochromat oil objective, NA 1.4 and super-resolution mode. For the analysis in Figures 2A–2C, seipin foci, mitochondria and LDs were segmented using Ilastik and the fraction of seipin foci overlapping with each compartment with at least one ~35 nm-sized pixel was analyzed CellProfiler coupled with custom Matlab software generated for post-processing. For the analysis in Figure 3D, mitochondria were segmented using Ilastik and the extracellular-background subtracted intensity of end-sfGFP-IP3R signal was measured within or outside mitochondria for each cell and this ratio was compared between all WT and seipin KO cells. For the analysis of seipin interactions with mitochondria (Figures 2F–2H), seipin foci were tracked manually in ImageJ FIJI. To be considered mitochondria-associated, a seipin foci had to clearly overlap with mitochondrial signal in at least three consecutive frames (1.5 or 1 sec apart). The motility of such tracks was measured in ImageJ FIJI and compared to the motility of seipin trajectories not overlapping with mitochondria.

Calcium measurements

In A431 cells, the measurements of cytoplasmic and mitochondrial matrix calcium (Ca^{2+}) in Figures 3G and 3H were conducted using the luminescent Ca^{2+} indicator protein aequorin, targeting either the cytoplasm or the mitochondrial matrix as previously described (Bonora et al., 2013), employing the multi-well based protocol as described (Bonora et al., 2013; Pulli et al., 2019). Briefly, A431 cells were plated on to 96-well plates (10000 cells/well) and incubated overnight. Thereafter, the cells were transfected (Turbofect, #R0531, Thermo Scientific;1μg plasmid/mL) and 24 hours following the transfection the cells were treated with IAA for 4 hours to

induce seipin degradation. Thereafter, the cells were washed and incubated in HBSS buffer (118 mM NaCl, 4.6 mM KCl, 10mM glucose, 20 mM HEPES,pH 7.4) supplemented with 5μM coelenterazine and 1 mM CaCl2 for one hour at RT in the dark to allow reconstitution of aequorin (Bonora et al., 2013). Thereafter the cells were briefly washed and transferred to a HIDEX Sense plate reader (HIDEXCorp., Turku, Finland) for the kinetic measurements of aequorin luminescence, and subjected to treatment with a combination of agonists (100 nM bradykinin, 50 μM ATP, 100 μM Histamine) inducing the Ca^{2+} flux. For calibration and analysis of the results, each measurement was concluded by treating the cells with the permeabilizing agent digitonin (100 μM) in presence of 10mM $CaCl_2$. Data were analyzed as described in (Bonora et al., 2013). For intracellular cytoplasmic calcium measurements in Figures S2A and S2B we used the fluorescent Ca^{2+}indicator Fura-2 AM. 10,000 cells per well were grown overnight on 96-well cell culture plates. Thereafter, the cells were loaded with, Fura-2 AM (2 μM, Life Technologies) as described previously(Cheyette and Gross, 1991). Following the Fura-2 AM loading, the cells were washed and incubated for 15 min in HBSS at room temperature in the dark, whereafter the kinetic fluorescence measurement were conducted by employing the HIDEX Sense plate reader system (HIDEX Corp, Turku, Finland) as described previously (Pulli et al., 2018).

For differentiated 3T3-L1 adipocytes, cells where washed with HBSS solution and then incubated 1 h at 37°c in experimental solution (900μl HBSS + 100 μL Reagent B, ENZO fluoforte kit)- containing 3 μM IP3 caged (Sichem, caged Ins(1,4,5)P3/PM [cag-iso-2-145]), 5 mM Fluo4 (Thermo Fisher) or 10μM Rhod2 (Thermo Fisher), 0.3% Pluronic acid F127. Cells where then washed in HBSS and fluorescence monitoring was performed with the Leica DMI 6000B time lapse microscope using the Metamorph (Molecular Devices) software. After obtaining basal fluorescence levels, UV flash photolysis ensures the rapid release of active IP3.

The measurements of mitochondrial Ca^{2+} in Figures 3I and 3J were performed using seipin degron control and seipin degron cells stably expressing CEPIA2mt, essentially as described (Suzuki et al., 2014). Briefly, cells were plated onto 96-well imaging plates overnight, then treated with IAA for 4 h in Fluorobrite medium containing 10% FBS. Prior to imaging, cells were transferred to Nikon Eclipse Ti-E microscope equipped with 40x air objective, NA0.75, Nikon Perfect Focus System 3, Hamamatsu Flash 4.0 V2 scientific CMOS and Okolab stage top incubator system and kept at +37 °c, 5% CO2. A field of view of cells was then imaged every 10 seconds, and after 40 seconds Fluorobrite medium containing simulants (100 nM bradykinin, 50 μM ATP, 100 μM Histamine final concentration) was added to the well and recording was continued for 260 seconds. The extracellular-background subtracted maximum increase in CEPIA-MT2 fluorescence/cell was measured using Image J FIJI and normalized to the mean fluorescence/cell prior to adding stimulants.

Mitochondrial metabolite quantification

For Figure 4H, metabolites were analysed by liquid chromatography-high resolution mass spectrometry (LC-HRMS). For Figure 4I, cells were cultured in DMEM serum-glutamine-sodium Pyruvate-phenol Red free supplemented with 25 mM of $^{13}C_6$-Glucose (Eurisotop CLM-1396-1) for 3 h. Cells were resuspended in 200 μL of absolute methanol then centrifugated for 15 min at 12000 rpm. Supernatants were dried at 45°C under a nitrogen stream and then resuspended in water containing 0.1% formic acid. Metabolites were quantified in samples by LC-HRMS. Analyses were performed on a Synapt G2 HRMS Q-TOF mass spectrometer equipped with an ESI interface operating in the negative mode and an Acquity H-Class UPLC device (Waters Corporation). Compounds were separated and the full-HRMS mode was applied for detection (*m/z* range 50-600) at a mass resolution of 25,000 full-widths at half maximum. The ionization settings were as follows: capillary voltage, 1 kV; cone voltage, 30 V; desolvation gas (N_2) flow rate, 900 L/h; desolvation gas/source temperatures, 550/120°C. Data acquisition and processing were achieved using MassLynx, TargetLynx and IsoCor (Millard et al., 2019) softwares. Metabolites compounds were detected by their calculated exact theoretical *m/z* with a mass tolerance of ± 0.001 Da (~ ±5 ppm). Metabolite's concentration in cell lysates were normalized with number of cells per sample (1million). Fractional enrichment of ^{13}C-glucose-derived glycolytic was evaluated by the addition of all ^{13}C-glucose-derived glycolytic metabolites relative to non-labeled metabolite abundances. Statistical analysis was performed using the Mann-Whitney test (Graphpad/Prism).

3'seq-RNA profiling

3'seq-RNA profiling was performed as described previously (Cacchiarelli et al., 2015). The libraries were prepared from 10 ng of total RNA in 4 μl. The mRNA poly(A) tails were tagged with universal adapters, well-specific barcodes and unique molecular identifiers (UMIs) during template-switching reverse transcriptase. Barcoded cDNAs from multiple samples were then pooled, amplified, and fragmented using a transposon-fragmentation approach that enriches for 3′ends of cDNA: 100ng of full-lentgth cDNAs was used as input to the Nextera DNA Sample Prep kit (ref FC-121-1030, Illumina) that enriches for 3′ends of cDNA. Library size was controlled on 2200 Tape Station System (Agilent Technologies). A library of 350–800 bp length was run on an Illumina HiSeq 2500 using a Hiseq Rapid SBS Kit v2-50 cycles (ref FC-402-4022) and a Hiseq Rapid PE Cluster Kit v2 (ref PE-402-4002) according to manufacturer's protocol (Denaturing and Diluting Libraries for the HiSeq® and GAIIx, Part # 15050107 v03 protocol, Illumina).

Raw fastq pairs matched the following criteria: the 16 bases of the first read correspond to 6 bases for a designed sample-specific barcode and 10 bases for a unique molecular identifier (UMI). The second read (58 bases) corresponds to the captured poly(A) RNAs sequence. We performed demultiplexing of these fastq pairs to generate one single-end fastq for each of the 96 samples. These fastq files were then aligned with bwa to the reference mRNA refseq sequences and the mitochondrial genomic sequence, both available from the UCSC download site.

RNA analysis

Total RNA from tissues was purified using Trizol (Life technology, les Ulis, France) according to the manufacturer's instructions. Total RNA from cell samples were purified with the NucleoSpin RNA II (Macherey Nagel, Hoerdt, France). Total RNA (500 ng) was reverse-transcribed and real-time quantitative PCR was performed using the TaqMan 7900 Sequence Detection System (Applied Biosystems, Warrington, UK). Primers were designed using the Primer Express 3.1 software (sequences available on request).

OCR measurements in lymphoblasts

For Figure 1D Oxygen consumption rate (OCR) in lymphoblasts was measured with a Seahorse XF96 Extracellular Flux Analyzer (Agilent). Before the analysis, the cells were maintained in their normal culture conditions. 30 min prior to OCR measurements, the cells were transferred to assay medium (XF base medium supplied with L-glutamine, 10 mM glucose and 1% FBS) and seeded to Poly-D-lysine coated XF96 Cell Culture Plates at density of 100 000 cells per well. OCR (pmol/min) measurements were corrected for cell number and normalized to OCR per cell of control cells.

Immuno-electron microscopy

For immuno-EM in A431 cells Figures 2D and 2E, cells were fixed with paraformaldehyde-lysine-periodate fixative (McLean and Nakane, 1974) (McLean and Nakane, 1974), permeabilized with 0.01% saponin (Sigma-Aldrich, Cat#S7900), and immunolabelled with anti-GFP antibody (Sigma ab290, 1:500, 1.5h), followed by 1.4 nm nanogold-conjugated anti-rabbit secondary antibody (Nanoprobes, Stony Brook, Cat#2004; RRID: AB_2631182, NY, 1:60 1 h). Nanogold particles were silver enhanced with HQ Silver kit (Nanoprobes, Stony Brook, NY), accordingly to manufacturer's instructions, and gold toned with 2% Na-Acetate, 0.05% $HAuCl_4$, and 0.3% $Na_2S_2O3 \cdot 5H_2O$. Cells were then post-fixed with 1% reduced osmium tetroxide in sodium cacodylate buffer, pH 7.4, for 1 h on ice, dehydrated through series of ethanol and acetone, and infiltrated with Epon (TAAB 812, Aldermaston, UK) for 2h prior to 14h polymerization at 60°C. 65-nm thin sections were cut using Leica UCT6 microtome and post-stained with uranyl acetate and lead citrate. EM imaging was done with Jeol JEM-1400 (Jeol Ltd., Tokyo, Japan), equipped with Gatan Orius SC 1000B bottom mounted CCD-camera (Gatan Inc., Pleasanton, CA). The distribution of the gold labeling quantified as described previously (Mayhew, 2011), using Microscopy Image Browser (MIB) software for segmentation and calculation (Belevich et al., 2016). 12 cells were randomly selected at low magnification. Higher magnification images were acquired at 8000x at north and south positions relative to the nucleus in these randomly selected cells. Images were calibrated, contrast normalized, and converted to 8-bit using MIB. To assign the gold particles to the respective organelle, following categories of cellular compartments were defined: endoplasmic reticulum (ER), ER-LD contact site, mitochondria-associated membranes (MAM), nuclear envelope (NE), lipid droplet (LD), mitochondria (Mito) and other. To estimate the area of the cellular compartments, the stereology tool of MIB (in MIB: Menu → Tools → Stereology) was used, where a grid with 230-nm spacing was placed on each image. Whenever a branch point fell on top of a cellular compartment, it was assigned to its respective category. Nuclear and extracellular area were excluded from calculations. Branch points per cellular compartment were calculated and the clusters of immuno-gold were annotated and assigned to corresponding cellular compartment. Labeling density, expected number of gold, and relative labeling index (RLI) were calculated as described previously (Mayhew, 2011). For immuno-EM data in Figures S1A and S1B, cells were treated and analyzed as described previously (Salo et al., 2016).

Transmission electron microscopy

For Figures 7C–7F, adipocyte tissue ($1mm^3$) was first fixed for 16 h at 4°C with 2.5% glutaraldehyde (LFG Distribution, Lyon, France) in 0.1M Sorensen buffer pH7.4. Samples were rinsed in 0.2 M cacodylate buffer, pH7.4, and subsequently postfixed with 2% osmium tetroxide/1.5% potassium ferrocyanide in 0.2 M cacodylate buffer, pH 7.4, for 45 min at room temperature. Samples were then rinsed with milliQ water and dehydrated in a graded series of ethanol followed by embedding in EMbed 812 epoxy resin (LFG Distribution), which was then polymerized at 60°C for 48h. Semithin sections (1μm-thickness) were cut with an EM-UC7 ultramicrotome (Leica, Nanterre, France), colored with 1% methylene blue/1% Azur II and observed with an Olympus AX-60 microscope (Olympus, Rungis, France) equipped with a QImaging QIClick digital CCD camera (QImaging, Surrey, Canada). Thin sections (60nm-thickness) were cut and observed with a Jeol JEM 1400 microscope (Jeol, Croissy sur Seine, France) operated at 120 KeV.

BSCL2 patient and control lymphoblasts (Figures 1A–1C) in RPMI medium were fixed by adding 2-fold strength fixative in 1:1 volume ratio to result in final concentrations of 2% glutaraldehyde, 2% formaldehyde, 2 mM $CaCl_2$ in 0.1M sodium cacodylate buffer, pH7.4. After 40 min fixation the cells were pelleted by centrifugation at 300g for 4 minutes. Samples were then osmicated with 1% osmium tetroxide for 1h, dehydrated through a series of ethanol and acetone prior to gradual infiltration into Epon (TAAB 812). The 60-nm-thick sections were cut from polymerized Epon, post-stained with uranyl acetate and lead citrate, and imaged with a Jeol JEM 1400 transmission electron microscope (Jeol Ltd., Tokyo, Japan) equipped with a bottom mounted CCD camera (Orius SC 1000B, Gatan Inc., AMETEK, CA). Images were acquired by systematic random sampling, and mitochondrial morphology and the presence of mitochondrial inclusions was analyzed manually.

Proteomic analysis

Proteomics analyses were performed at the 3P5 proteomics facility. Briefly: pH 2.0-eluted proteins from immuno-precipitates were submitted to thiol-reduction and alkylation using 20mM TCEP and 50mM chloroacetamide (both from Sigma) for 5 min at 95°C. Proteolysis for *bottom-up* proteomics experiments was performed with trypsin (sequencing-grade from Promega), by the FASP and

stage-tips methods (Wisniewski et al., 2009). Peptides were cleaned and fractionated with C_{18} and SCX StageTips, respectively. Mass spectrometry (MS) analysis of the peptide mixtures was performed with an U3000-RSLC nano-liquid chromatographer (nLC) hyphenated to an Orbitrap Fusion mass spectrometer (both from Thermo Scientific). The data were acquired throughout the elution process and the MS operated in a data dependent scheme with full-MS scans acquired with the orbitrap analyzer, followed by as many HCD MS/MS as possible in 5 seconds time (top speed mode) and detection was performed in the linear trap analyzer. MS/MS spectra were measured on the most abundant ions detected in the MS scan. The following settings were used - for full-MS: AGC at 2.10^5, resolution: 60,000 full-widths at half maximum, *m/z* range 350-1500, within 60 ms Maximum Ion Injection Time (MIIT). –for fragmentation or MS/MS, precursors over 1.10^4 intensity, with a charge state from 2 to 7 were filtered in the quadrupole window within 1.6 Th window. A dynamic exclusion time was set at 30 s. HCD was performed with NCE at 30%, fragments were detected in the ion trap with AGC Target at 2.10^4 and within 100ms MIIT. Data were analyzed with Mascot version 2.5.1 (Perkins et al., 1999). The database used was a concatenation of *Mus musculus* sequences from the reviewed Uniprot-Swissprot database (UniprotKB, release 2018-03 (16,975 sequences from *M. musculus*) and the CRAP database (Mellacheruvu et al., 2013). Cysteine carbamidomethylation was set as a constant modification while methionine oxidation was set as variable modifications. The MyPROMS database software (Poullet et al., 2007) was used for sample comparison. The false discovery rate (FDR) was kept below 1% for peptides and protein identification required at least two such peptides matching the same protein in at least one sample of the compared sample set.

QUANTIFICATION AND STATISTICAL ANALYSIS

Analysis of 3'seq-RNA profiling

Gene expression profiles were generated by parsing the alignment files (.bam) and counting for each sample the number of UMIs associated with each gene. Reads aligned on multiple genes, containing more than three mismatches with the reference sequence or having a polyA pattern were discarded. Finally, a matrix containing the counts of all genes on all samples was produced. The expression values, corresponding to the absolute abundance of mRNAs in all samples, was then ready for further gene expression analysis. The R package deseq2 (Love et al., 2014) was used for the differential analysis.

We applied *MaSigPro* (Conesa et al., 2006) to the log-transformed transcriptomic data to identify genes with significant differences in response as a time-dependent function of the group. By using the default parameters and a quadratic regression model, we first identified genes with profiles showing significant expression differences from *CRE.Tamox.* We used the method of Benjamini and Hochberg (Benjamini and Hochberg, 1995) to estimate the false discovery rate (FDR) to control for false positives (FDR < 0.05). We next used a backward step-wise selection procedure to calculate best regression models for each gene, resulting in 418 genes that were selected for clustering analysis.

To cluster selected genes depending on their expression profiles, we performed *Weighted correlation network analysis (WGCNA)* (Langfelder and Horvath, 2007). An unsigned adjacency measure for each pair of genes was calculated by raising the absolute value of their Pearson correlation coefficient to a power of a parameter p. The later (p=12) was calculated using the algorithm from (Zhang and Horvath, 2005). The obtained adjacency matrix was then used to calculate the *topological overlap measure* (*TOM*) which, for each pair of genes, takes into account their weighted pairwise correlation (direct relationship) and their weighted correlations with other genes in the network (indirect relationship). Using a *hierarchical clustering* based on the *TOM* measure, we identified six genes' modules, each shows a significantly different pattern.

Statistical analysis

All data are reported as mean±SEM (standard error of mean). Data sets were analyzed for statistical significance with non-parametric and parametric tests as indicated in the Figure legends. For AUC analyses, t-test was performed using mean and standard deviation of each group. Two-way ANOVA analysis was used as specified and significance represented is the interaction between the two parameters (usually the biological group and the studied parameters). All the analyses were performed with GraphPad Prism.